Available online at www.sciencedirect.com
ScienceDirect
International Journal of Heat and Fluid Flow 28 (2007) 229–248
International Journal of HEAT AND FLUID FLOW
www.elsevier.com/locate/ijhff

Vortex breakdown in a cylinder with a rotating bottom and a flat stress-free surface

E. Serre *, P. Bontoux

MSNM-GP UMR 6181, CNRS/Aix-Marseille-Université, La Jetée-Technopôle de Château-Gombert, 38 rue Frédéric Joliot-Curie, 13451 Marseille Cedex 20, France

Received 11 January 2005; received in revised form 22 April 2006; accepted 28 April 2006
Available online 10 July 2006

Abstract

Vortex breakdown and transition to time-dependent regimes are investigated in a cylinder ($H/R = 4$) with a rotating disk and a free-surface. The aim of this study is to show how, by changing upstream conditions it is possible to alter on the flow, particularly the vortex breakdown process. The understanding of such effects on vortex breakdown is very useful in the development of a control strategy in order to intensify or remove the phenomenon. The flow dynamics are explored through numerical solution of the three-dimensional Navier–Stokes equations based on high-order spectral approximations. The use of a flat, stress-free model for the air/water interface is shown to be entirely satisfactory at least for moderate Reynolds numbers. A particular interest of these results is to show how the bubble related to the vortex breakdown becomes attached to the free-surface and grows in diameter as the Reynolds number is increased, $Re \geqslant 2900$. Such a phenomenon removes the cylindrical vortex core upstream of the breakdown which is usually included in classical theories based on idealized models of vortex flows. The flow is shown to be unstable to three-dimensional perturbations for sufficiently large rotation rates. The bifurcated state takes the form of a $k = 3$ rotating wave at $Re = 3000$. The existence of the free-surface promotes the onset of periodicity, with a critical Reynolds number about 15% lower than in the case with a rigid cover. Moreover, the successive bifurcations occur over a much shorter range of Reynolds numbers and lead rapidly to a multi-frequency regime with more than five different frequencies. In the unsteady regime, the vortex breakdown is characterized by an elongated, asymmetric recirculation zone, attached to the free-surface and precessing around the axis of the container. By increasing the rotation, the circular stagnation line on the free-surface takes a more irregular form and starts to move around the axis of the cylinder in the same sense as the rotating disk. Finally, our results show that the vertical boundary layer controls both the vortex breakdown process and the transition to unsteadiness.

Keywords: Nanofluid; Heat transfer enhancement; Laminar flow; Nanoparticle

1. Introduction

When increasing the swirl in a rotating flow a point is reached where the adverse pressure gradient along the jet axis cannot be further overcome by the kinetic energy of the fluid particles flowing in the axial direction, and a recirculation flow zone is set up. Although flow reversal does not necessarily occur in helical and turbulent vortex breakdown (see Sarpkaya, 1995), the development of such a recirculation zone and flow reversal can define a vortex breakdown, bringing the vortex breakdown to an internal flow separation (Leibovich, 1978). This definition is currently considered in most cases in confined cavities, in which the vortex breakdown is often assimilated into one or more recirculation bubbles following the pioneering experimental investigations of Escudier (1984).

The motion of a viscous fluid contained in a closed cylinder, with a rotating disk lid which recirculates the flow inside the container, poses an attractive example of confined swirling flow and provides very well controlled conditions, particularly so for numerical studies. The major characteristics of the flow are known to be determined by

* Corresponding author. Tel.: +33 4 91 11 85 35; fax: +33 4 91 11 85 02.
E-mail address: serre1@L3m.univ-mrs.fr (E. Serre).

0142-727X/$ - see front matter
doi:10.1016/j.ijheatfluidflow.2006.04.004

Nomenclature

H, R	height and radius of the cylinder
Ω	rotation speed of the bottom end wall
v	dynamic viscosity
g	gravitational acceleration
$\Gamma = H/R$	aspect ratio
$Re = \Omega R^2/v$	Reynolds number
$Fr = \Omega^2 R^2/gH$	Froude number
(r^*, θ, z^*)	dimensional cylindrical coordinates system in the absolute frame of reference
(r, z)	dimensionless radial and axial coordinates
$\bar{r}$	dimensionless normalized radius in $[-1, 1]$
$V = (u, v, w)$	dimensionless velocity
p	dimensionless pressure
h, e	axial length and maximum radial extension of the vortex breakdown
L	distance along the axis from the centre of the bottom rotating disk to the upstream fixed point of the bubble

two dimensionless parameters: the aspect ratio ($\Gamma = H/R$) and the rotational Reynolds number ($Re = \Omega R^2/v$), where H and R are respectively, the height and the radius of the cylinder, Ω the angular velocity of the top end wall, and v the kinematic viscosity of the fluid.

For certain combinations of (Γ, Re), the confined vortex can undergo breakdown. One of the particular interests is that vortex breakdown may be observed under laminar and steady conditions, without the influence of turbulence, contrary to the case of vortex tubes or in trailing vortices. Moreover, this kind of flow provides a very interesting way for studying transition to turbulence in finite-dimensional systems (Sørensen and Christensen, 1995).

The fundamental nature of the flow (axisymmetric or three-dimensional) has been, at least until recently, the subject of considerable controversy. Using a stability analysis Gelfgat et al. (2001) showed that in the range, $1.63 \leqslant \Gamma \leqslant 2.76$, the dominant perturbation mode is axisymmetric ($k = 0$) while outside this range, the instability is non-axisymmetric as supported by three-dimensional computations of Navier–Stokes equations (see Blackburn and Lopez, 2000; Marques and Lopez, 2001; Serre and Bontoux, 2002). In contrast, Spohn et al. (1998) in experiments and Sotiropoulos and Ventikos (2001) in computations clearly established the asymmetry of the steady vortex bubble at the downstream end. Sotiropoulos and Ventikos (2001) reproduced Lagrangian images of the breakdown bubbles in remarkable agreement with the visualizations photographs of Spohn et al. (1998). What was observed by Sotiropoulos and Ventikos (2001) from Eulerian comparison measures, is that the asymmetry mode in the three-dimensional flow field may be very small but it could nevertheless have a large impact on the Lagrangian dynamics of an axisymmetric flow. Such finding could explain the discrepancy observed between the manifold structures of axisymmetric vortex breakdown in steady regimes observed from numerical integrations of the three-dimensional Navier–Stokes equations (Blackburn and Lopez, 2000; Marques and Lopez, 2001; Serre and Bontoux, 2002) and those of the recent experiments of Spohn et al. (1998) and computations of Sotiropoulos and Ventikos (2001). The topology of the steady vortex breakdown has been very recently specified numerically by Sotiropoulos et al. (2001) and experimentally by Sotiropoulos et al. (2002), and chaotic particle paths were also emphasized within the bubble.

In spite of numerous studies, all the details concerning the question of the symmetry breaking have not been explained. The symmetry breaking could be related to the centrifugal instability, leading an asymmetric flow separation on the container wall as observed experimentally by Spohn et al. (1998) and numerically by Sotiropoulos and Ventikos (1998, 2001). Nevertheless, Sotiropoulos and Ventikos (1998, 2001) showed that in their computations the separation is forced by the distorted structure of their Cartesian numerical grid. In contrast, for Blackburn and Lopez (2000), and Marques and Lopez (2001) this symmetry breaking of the flow is attributed to an inflectional instability of the swirling jet produced by the turning of the Ekman layer on the stationary vertical sidewall. This result looks to be confirmed by a recent stability analysis of Blackburn (2002) carried out in a cavity of aspect ratio $\Gamma = 2.5$ and at $Re = 4000$.

In all studies mentioned above, the rigid end walls impose the no-slip condition on the flow and thus force the formation of three-dimensional boundary layers, which interact with the swirling motion in the inner part of the container. In this way, the characteristics of the vortex flow are determined by the boundary conditions, and by changing them it is possible to act on vortex breakdown conditions. Following this idea, a number of boundary conditions variations have been recently studied: the flat rotating bottom cover has been replaced by a cone (Pereira and Sousa, 1999), or a rod has also been added at the axis (Mullin et al., 2000). The aim of the present study is to investigate the consequence on the flow structure and on the conditions of vortex breakdown, when the upper boundary no-slip condition is replaced by a flat free-surface. Studies of rotating flows in containers with a free-surface are scarce. Experimentally (Spohn et al., 1993) the flow structure including vortex breakdown has been considered in a container of aspect ratio $\Gamma \leqslant 4$ and $Re \leqslant 4000$ and more recently in a $\Gamma = 2$-cylinder (Hirsa et al., 2002). Spohn et al. (1993) particularly emphasized breakdown bubbles attached at the free-surface in steady regimes. Indeed, these authors observed that the use of water in experiments made the flow very sensitive to perturbation

for $\Gamma > 3$ and $Re > 1500$, external noise leading to dramatic changes of the flow structure. Nevertheless, in a $\Gamma = 2$-cavity, Young et al. (1995) experimentally observed a transition route from a steady state to a chaotic regime through period-doublings as Re is increased beyond 2000. In an identical cavity, Hirsa et al. (2002) have more recently shown that the symmetry is breaking to a $k = 4$ rotating wave and they have conjectured that these period-doublings correspond to precession periods of the azimuthal mode $k = 4$, 2 and 1, successively.

Existing numerical approaches were mainly axisymmetric (see Daube, 1991; Spohn and Daube, 1991; Brøns et al., 2001) while we can expect that the transition to time-dependent flows is related to three-dimensional modes of instability, at least in large aspect ratios cavities (Spohn et al., 1998). Nevertheless, Brøns et al. (2001) using a topological approach, obtained a list of possible bifurcations of streamline structures from varying the parameters (Re, Γ). These bifurcations are shown to be of a purely topological nature and are not related to changes in stability of the steady flow. For higher Reynolds numbers, Brøns et al. (2001) have also numerically investigated the transition to time-dependent solutions (axisymmetric) in cavities of aspect ratios $\Gamma \leqslant 3$, and have shown that the stability limit for steady flow is established as a Hopf bifurcation. The symmetry breaking was recently explored experimentally and numerically by Lopez et al. (2004), in an extended problem of flow in a cylinder of length $2H$, but driven by two co-rotating rigid end walls. In this configuration the mid-plane is a reflection boundary that corresponds to a flat, stress-free interface. Their study showed that for a shallow system ($\Gamma = 0.26$), the flat stress-free model fails to capture the primary instability by imposing a hidden symmetry condition on the numerical solutions, restricting the solution to an even z-parity subspace. Nevertheless in the deep system ($\Gamma = 2$), they obtained good agreement between experiments and computations and so the imperfections in the physical free-surface experiment do not qualitatively change the dynamics.

In order to provide additional information regarding the vortex breakdown and the three-dimensional behaviour of these kinds of flows, three-dimensional simulations using a high-order numerical method have been carried out in a cylinder with a rotating bottom and a free-surface. The accurate numerical simulation of swirling flows exhibiting vortex breakdown is particularly demanding, since it requires the solution of the full Navier–Stokes equations in cylindrical coordinates for three-dimensional, unsteady flows. A $\Gamma = 4$-cylinder (as in Serre and Bontoux, 2002) was selected, allowing a comparison between both rigid and free-surface end wall conditions. The three-dimensional Navier–Stokes equations are solved using a pseudo-spectral Chebyshev–Fourier method associated with a multi-step time scheme detailed in Serre and Pulicani (2001).

In the present study, the occurrence of the vortex breakdown has been accurately analyzed, especially the attachment of the bubble on the free-surface. A time periodic solution has been obtained at $Re = 3000$ and a multi-periodic solution has been observed at a slightly larger Reynolds number $Re = 3150$ showing the unstable character of this configuration. The time-dependent flows are shown to be related to different modes of instability and characterized by an asymmetric vortex breakdown attached to the free-surface and precessing around the axis.

The paper is organized as follows. The mathematical model and numerical solution technique are described in Sections 2 and 3. Section 4 presents numerical details, and the flat-stress free model is validated in Section 5. The numerical results are given in Section 6 and are analysed in detail and compared with other investigations in Section 7. Concluding remarks are given in Section 8.

2. Geometry and mathematical model

The configuration that is considered is a cylinder at rest of radius R and height H. The end wall at $z^* = -H/2$ rotates at an angular velocity Ω while the end wall at $z^* = H/2$ is assumed to be stress-free. The flow is governed by the incompressible three-dimensional Navier–Stokes equations written in cylindrical coordinates (r^*, θ, z^*) in an absolute frame of reference, according to the velocity–pressure formulation. Parameters characteristics of the physical problem are the Reynolds number $Re = \Omega R^2/\nu$ and the aspect ratio $\Gamma = H/R$.

The scales for the dimensionless variables of space, time and velocity are $[H/2, \Omega^{-1}, \Omega R]$, respectively. The dimensionless radius $(0 \leqslant r \leqslant 2/\Gamma)$ has been normalized on $[-1, 1]$, a requisite for the use of Chebyshev polynomials: $r = \Gamma^{-1}(1 + \bar{r})$, $\bar{r} \in [-1, 1]$.

No-slip boundary conditions apply at each impermeable wall. Thus $u = w = 0$ on all rigid walls. For the azimuthal velocity, the boundary conditions are $v = 0$ on the cylinder wall and $v = 0.5 \times (1 + \bar{r})$ on the rotating disk $(z = -1)$. The singularity at the junction of the stationary cylinder with the rotor is treated appropriately, by employing a boundary layer function, $v_\mu = \exp(-(z - 1)/\mu)$, where μ is an arbitrary shape parameter. It was shown for equivalent Reynolds numbers in Serre and Bontoux (2002) that this function with $\mu = 0.006$ provides a reasonable representation of the size of the gap that would be necessary in an experimental system, while retaining spectral accuracy.

The free-surface at the top $(z = 1)$ will be assumed flat. This assumption can be considered as reasonable because in experiments of Spohn et al. (1993) the Froude number ($Fr = \Omega^2 R^2/gH$ where g is the gravitational acceleration) remains small ($0.002 \leqslant Fr \leqslant 0.017$), involving very small deformations of the free-surface which do not exceed 1% of the cavity height H. Further, any surface tension will be neglected, so the surface is a pure slip boundary ($\partial u/\partial z = \partial v/\partial z = 0$ and $w = 0$). We mention that this stress-free model might impose hidden symmetries leading to spurious solution branches (see details in Crawford et al., 1993). Nevertheless, recent computations of Lopez et al. (2004)

have shown that this flat stress-free condition does not impose hidden symmetry in a deep cylinder ($\Gamma = 2$) and gives a good quantitative agreement with experiments in contrast to a shallow system ($\Gamma = 0.25$).

The initial condition corresponds to no motion in the meridional plane and to a linear shear profile for the azimuthal velocity: $u = 0$; $w = 0$; $v = 0.25 \times (1 + \bar{r})(1 - z)$, for $-1 \leqslant \bar{r}, z \leqslant 1$.

3. Numerical method

The numerical solution is based on a pseudo-spectral collocation-Chebyshev in both radial and axial directions (r, z) and considering the 2π-periodicity of the solution in this configuration a Fourier–Galerkin method is used in the azimuthal direction (Peyret, 2002). The mesh grid is defined by the Gauss–Lobatto collocation points along (r, z), $r_i = \cos(i\pi/N)$ $i = 1, \ldots N$, $z_j = \cos(j\pi/M)$ $j = 1, \ldots, M$ and an equidistant distribution of points in the azimuthal direction, $\theta_k = 2k\pi/K$ $k = 0, \ldots, K-1$, with N, M, and K being the number of radial, axial, and azimuthal points for the spatial mesh. Then, the approximation of flow variables is given by:

$$\Psi_{NKM}(\bar{r}, \theta, z, t) = \sum_{n=0}^{N} \sum_{m=0}^{M} \sum_{k=-K/2}^{K/2-1} \hat{\Psi}_{nmk}(t) T_n(\bar{r}) T_m(z) \mathrm{e}^{ik\theta}, \quad (1)$$

where, $\Psi = (u, v, w, p)$, $(\bar{r}, z, \theta) \in [-1, 1]^2 \times [0, 2\pi]$, T_n, T_m are the Chebyshev polynomials $(T_n(\bar{r}) = \arccos(n \cos \bar{r}))$ and $\hat{\Psi}_{nmk}(t)$ the Fourier coefficients.

The choice takes into account the orthogonality properties of Chebyshev polynomials and, in particular, provides exponential convergence – referred to as spectral accuracy (Serre and Pulicani, 2001; Raspo et al., 2002). The high-order accuracy of these methods ensures an accurate description of the secondary flows of weak intensity compared to the external basic flow (Serre et al., 2001; Serre and Bontoux, 2002). Moreover, the use of the Gauss–Lobatto collocation points directly ensures high accuracy of the solution inside the very thin wall layers and in the neighbourhood of this axis.

The time scheme is semi-implicit and second-order accurate. It corresponds to a combination of the second-order backward differentiation formula for the time derivative term and of the Adams–Bashforth scheme for the nonlinear terms. Then, the dimensionless Navier–Stokes equations are written in the domain as:

$$\frac{3V^{n+1} - 4V^n + V^{n-1}}{2\delta t} + 2(V \cdot \nabla V)^n - (V \cdot \nabla V)^{n-1} = -\nabla p^{n+1} + Re^{-1} \Delta V^{n+1} \nabla \cdot V^{n+1} = 0, \quad (2)$$

where $V = (u, v, w)$ is the velocity vector, p is the pressure and δt is the time step such that $t^n = n\delta t$.

The velocity–pressure coupling is performed with a projection algorithm developed by Gresho and Sani (1987) for finite elements and applied here for 3D spectral calculations. This algorithm has been improved with an extension at each time step of a preliminary pressure, previously only estimated at the initial step. This procedure allows a possible temporal evolution of the normal pressure gradient at the boundaries. This pressure predictor is computed for by means of an elliptic equation obtained by taking the divergence of the incompressible Navier–Stokes equations (Eq. (1)). As proposed in Gresho and Sani (1987), Neumann boundary conditions for the pressure can be obtained by projecting the Navier–Stokes equations (Eq. (1)) normally to the wall in which the diffusive term is evaluated using an Adams–Bashforth scheme.

When using cylindrical coordinates to calculate the solution of the three-dimensional Navier–Stokes equations in a cylinder, the complexity is further increased by the singular behavior of the coefficients when the radial coordinate tends to zero. Indeed, the Fourier–Galerkin approximation leads to a set of elliptic equations for each Fourier wave to be solved in a two-dimensional domain depending on the two non-periodic directions. To obtain the solution of these equations boundary conditions are required at the axis and at the wall. At the wall these conditions are given by the physical problem and at the axis they are imposed by the uniqueness of the solution except for the first Fourier mode. As in Pulicani and Ouazzani (1991), a change of dependent variables (velocity, pressure) was used to enforce a boundary condition at the axis for this first mode: $\tilde{V} = \Gamma^1(\bar{r} + 1)V$ and $\tilde{p} = \Gamma^1(\bar{r} + 1)p$. This variable change yields the conditions $\tilde{u} = \tilde{v} = \tilde{w} = \tilde{p} = 0$ at the axis $\bar{r} = -1$. It is easy to obtain V and p from $\tilde{V}$ and $\tilde{p}$, except at $\bar{r} = -1$, but the numerical method does not require this value. Nevertheless, in order to graphically represent the solution, different techniques for estimating the axis value are proposed in Serre and Pulicani (2001).

4. Numerical details

The grid currently used is 64×96 in the (r, z) plane with 64 Fourier modes in the azimuthal direction as in Serre and Bontoux (2002) who used a rigid cover instead of a free-surface and the same aspect ratio. The grid sensitivity of the numerical method was previously evaluated in the cavity with a rigid cover Escudier, 1984 and the solutions were shown to be grid independent. Moreover, the comparative results were in good agreement with various well documented test cases (see Escudier, 1984; Marques and Lopez, 2001). In the present configuration, different refinements have been also tested in the steady flow regime and the solution at $Re = 2600$ has been recomputed with higher resolutions in the meridian plane: 96×96 and 64×128 in the (r, z)-plane. The space and time scales of the solution, as exemplified by the maxima of the velocity component, alter by less than 0.1% with the refinement in the grid spacing. Consequently, the grid of $64 \times 96 \times 64$ points in (r, z, θ) directions, respectively, looks fine enough for the rotation considered in this study and corresponds to a compromise between the computational cost of the solution and the high accuracy required in the thin boundary layers and in

the narrow region close to the axis. The time steps adopted is $\delta t = 2 \times 10^{-2}$.

For the time-dependent solutions, the computing time is determined around the largest characteristic time in rotating flows, i.e., the viscous diffusion time ($t_v = H^2/v$); the dimensionless viscous time is equal to ΓRe and the largest value is 12 600. Around one diffusion time, viscous effects have permeated the entire cavity and the small residual oscillations are strongly damped. Steady solutions are expected when the convergence rate becomes smaller than the relevant criterion $|V^{n+1} - V^n|/\delta t \leqslant 10^{-5}$, where the superscripts $n+1$ and n correspond to the stages $(n+1)\delta t$ and $n\delta t$, respectively.

The three-dimensional nature of the solution is monitored through a time series of E_k:

$$E_k(t) = \sum_{i=1}^{N} \sum_{j=1}^{M} \hat{u}_k(r_i, z_j, t)\bar{\hat{u}}_k(r_i, z_j, t),$$

which is an approximate measure of the discrete spectral energy in each Fourier mode k, where $\hat{u}_k(r_i, z_j)$, is the value of the kth Fourier mode of the velocity at the collocation points (r_i, z_j), and $\bar{\hat{u}}_k$ is the complex conjugate of $\hat{u}_k$.

The performance of the solver has been optimised with respect to a vector-parallel supercomputer, here a NEC SX5. The code was carried up to high speed crest performances as we obtained about six gigaflops and a reference CPU time less as 10^{-6} s/mesh point/δt. These code capabilities made possible the efficient computation of the high resolution time-dependent solutions and to reach sufficiently large simulation times to make the results of physical relevance.

5. Qualification of the flat stress-free model

The ability of the numerical method to ensure an accurate description of rotating flows with walls has been already shown in Serre et al. (2001) and Serre and Bontoux (2002). In this Section, we show the ability of the flat stress-free model of the free-surface to capture the general features of the flow in deep cylinders. Then, preliminary computations have been carried out for a well documented test case corresponding to a cavity of smaller aspect ratio, $\Gamma = 2$. The evolution of the central flow structure in steady regimes with increasing Re–$Re = 1740$ is in good agreement with the experimental observations of Spohn et al. (1993) and the primary instability related to flow symmetry breaking is obtained at $Re > 1900$ as in Lopez et al. (2004).

(1) The number and the position of the breakdown bubbles in stationary flows occurring in a $\Gamma = 2$-cavity have been found to be in very good agreement with the experiments of Spohn et al. (1993), where the one-bubble vortex breakdown occurs close to the free-surface at $Re = 1210$ and merges with the top free-surface at $Re = 1420$ (Fig. 1). The characteristic lengths of the breakdown bubble in stationary flows inside a $\Gamma = 2$-cavity are found to be consistent with the available experimental data measured from the visualizations displayed in Fig. 2(d)–(f) in Spohn et al. (1993, see in Table 1). In the present study, the onset of the steady one-bubble vortex breakdown arises in the basic flow at a slightly smaller Reynolds number than in experiments, at about $Re = 1180$. The merging of this bubble with the free-surface is numerically determined between $Re = 1350$ and 1400 in good agreement with experiments as well. Once adjacent to the free-surface, the diameter of the bubble begins growing as Re is further increased up to $Re = 1740$ (Table 1), in good agreement with the observations of Spohn et al. (1993).

(2) The bifurcation examined by Lopez et al. (2004) (obtained numerically at $Re = 1910$ and experimentally at about $Re = 2000$) has been well reproduced at a slightly higher Reynolds number, $Re = 2050$. This first transition to unsteady flow occurs via a Hopf bifurcation to a rotating wave $k = 4$, as in the experimental and numerical work of Lopez et al. (2004). The vortex breakdown remains axisymmetric and attached to the free-surface and the only departure from symmetry occurs in the meridional plane. Rolls develop in the vertical layer along the container wall and travel upstream to the free-surface. When these structures reach the core region, they combine into a helical vortex pattern and go down along the axis before vanishing in the vicinity of the rotating disk (Fig. 2(a)).

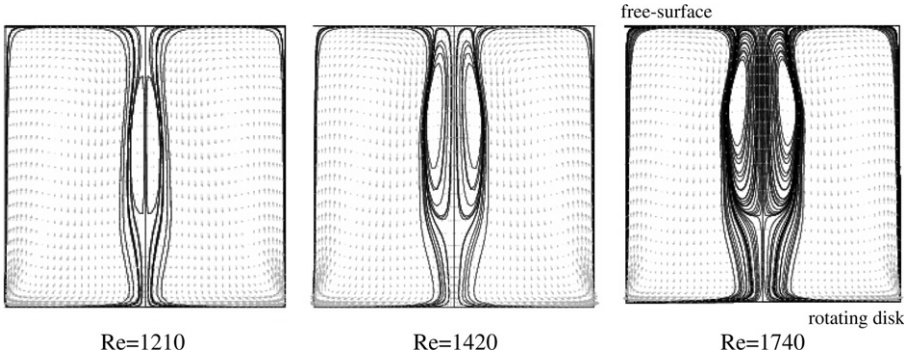

Fig. 1. Velocity vector field and predicted streaklines of particles in bold in meridional plane $(r, 0, z)$ in a $\Gamma = 2$ cylinder and at different Reynolds numbers Re. Particles are released just below the free-surface (at the top) and at different radial positions around the axis ($r^* < R/3$).

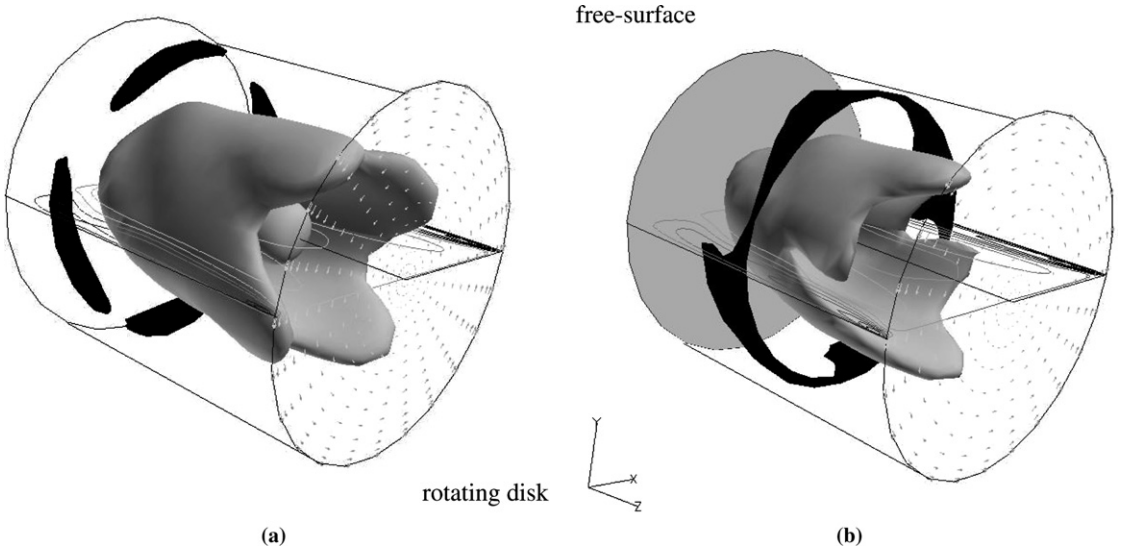

Fig. 2. Three-dimensional flows with an axisymmetric vortex breakdown bubble attached to the free-surface in a $\Gamma = 2$-cylinder. (a) A $k = 4$ rotating wave at $Re = 2050$. Instantaneous isosurfaces $w = -0.037$ (grey) and $w = 0.025$ (black) (restricted in the range $0.8 \leqslant z \leqslant 1$). Along the axis the vortex breakdown is characterized by the isosurface $w = 0$. (b) $k = 4$ and $k = 2$ waves at $Re = 2150$. Instantaneous isosurfaces $w = -0.0385$ (grey) and $w = 0.0285$ (black) (restricted in the range $0.1 \leqslant z \leqslant 1$). Instantaneous isolines of $w = \pm 0.05$ in the meridional planes and velocity vector field at the rotating disk.

(3) The secondary bifurcation occurs at the slightly higher Reynolds number $Re = 2150$ where the $k = 4$ rotating wave becomes unstable to a $k = 2$ azimuthal mode. As in Lopez et al. (2004), the $k = 2$ mode is dominant in the central core region while the $k = 4$ mode remains more in the outer flow region. The flow structure is illustrated in Fig. 2(b) by showing the isolines of axial velocity at different axial positions.

The complexity of the phenomena and of the dynamical processes that are simulated in this section, are considered as establishing the quality and the accuracy of the solution solver. These results provide validation of the numerical modelling to reproduce free-surface cylinder flows in deep cavities.

6. Results

In order to explore parameter space, computations have been conducted by varying the rotation rate while maintaining a fixed aspect ratio $\Gamma = 4$. For the basic state ($Re = 2200$), the calculations were initiated from rest by impulsively spinning-up the rotating lid. At larger rotation rates, the computational strategy consisted of initializing the next solution at larger Re with the computational solution obtained at the lower value of Re. In all these results, no three-dimensional perturbation was added.

The scenarios of the onset of vortex breakdown and unsteadiness patterns are introduced in Sections 6.1 and 6.2, respectively. We will identify the process as "detached" vortex breakdown if both stagnation points are on the axis and "attached" vortex breakdown when the bubble merges with the free-surface, one stagnation point at least being located on the surface.

6.1. Basic state

Starting from an initial state at rest, the bottom end wall starts rotating instantaneously at $Re = 2200$. After a short transient time, all non-axisymmetric modes decayed until their energies E_k, $k \neq 0$ reached machine zero level. Then, the resulting solution is axisymmetric and steady (the velocity components changing by less than 10^{-12} over a time interval of $\delta t = 10$) without vortex breakdown. This solution is considered to be the basic flow. It differs from the solution obtained by Serre and Bontoux (2002) in the rigid cover cylinder in that there is no longer a Bödewadt boundary layer along the stationary end wall.

As in the case of an infinite disk, when the rotating end wall is impulsively started, a thin Ekman boundary layer is formed which acts as a pump (known as Ekman pumping) drawing in fluid axially and driving it away in centrifugal spirals (Rogers and Lance, 1960). In a closed container, this fluid swirls along the stationary vertical wall to the free-surface and forms a boundary layer which grows following the main flow direction. As shown by the velocity field displayed in Fig. 3(a), the non-constant thickness of this boundary layer acts on the flow and plays to some extent the role of a vertical diverging tube (represented in Fig. 3(a) by constructing the line $w = 0$ in a meridional plane) imposing a slight adverse pressure gradient ($\partial p/\partial z \leqslant 0$) along its axis as shown on Fig. 4(a) for different Reynolds numbers. At $Re = 2200$, the negative pressure gradient in the lower half part of the cavity ($-1 \leqslant z \leqslant 0$) is associated with a deceleration of the axial velocity w (Fig. 4(b)). At higher Reynolds numbers ($Re = 2600$ and $Re = 2900$), the pressure gradient is now negative over

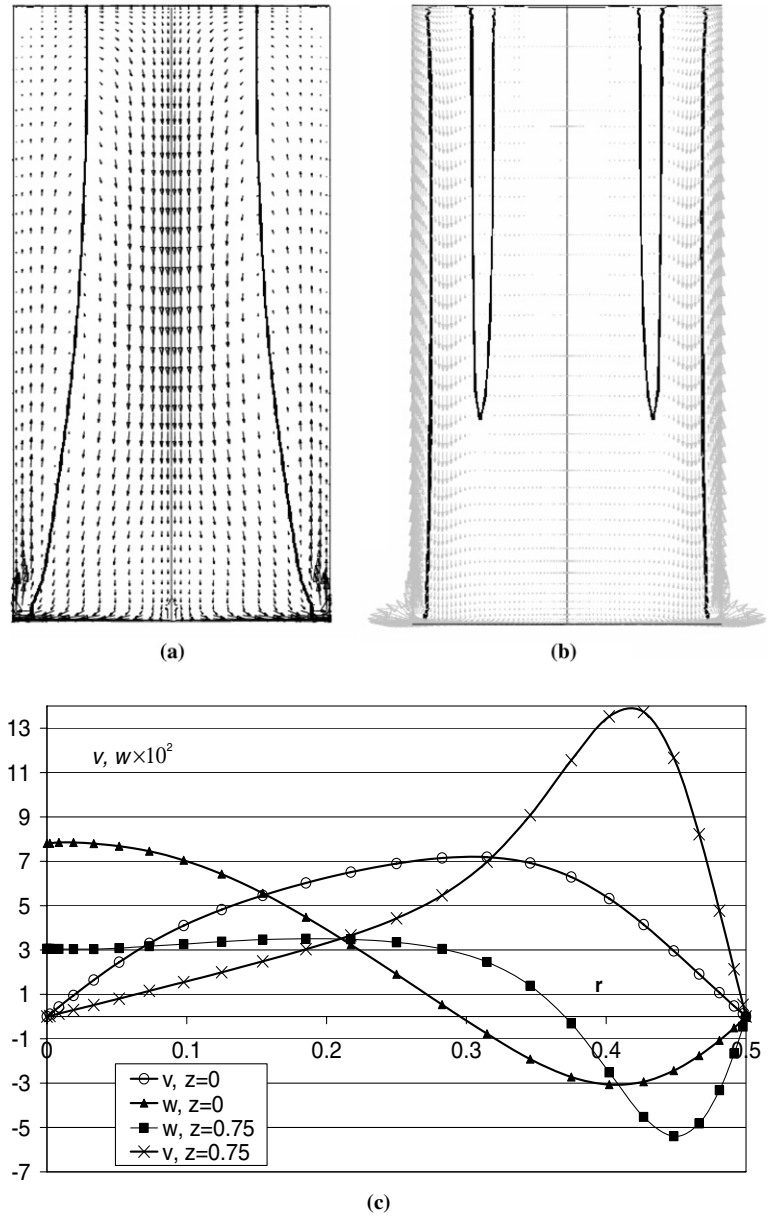

Fig. 3. Steady and axisymmetric base flows in the meridional plane (r, 0, z). (a) Velocity field and isoline $w = 0$ emphasizing the diverging tube-like flow at $Re = 2200$. (b) Velocity field and isoline $w = 0$ at $Re = 1500$ in a container with a vertical slip-surface imposing no tangential stress. (c) Radial profiles at $Re = 2200$ of the vertical (w) and azimuthal (v) components of the velocity at mid-height ($z = 0$), and close to the rotating disk ($z = -0.75$) showing uniform and jet-like profiles.

the entire height of the cavity and the axial velocity can ultimately reach negative values.

Near the top free-surface, the radial motion is only caused by the pumping effect of the rotating disk boundary layer. In contrast to the cylinder with a rigid cover, the fluid is not supposed to be decelerated along the free-surface which imposes here no tangential stress (slip condition). Because of this, no boundary layer is formed and the fluid spirals inward along the surface and again turns in the axial direction, towards the rotating disk. Large radial velocities are then restricted to both rotating-disk and free-surface flow regions bounding the flow domain.

Consequently, the flow inside the cylinder is driven and mainly determined by the axial component of the velocity w and by the azimuthal component v depending on the rotation speed of the disk, Ω. Radial profiles of the two velocity components measured in the vortex core close to the rotating disk and at mid-height show characteristics of a uniform and a jet-like axial flow, respectively (Fig. 3(c)). The interplay between these two components can be characterized by a swirl parameter S, defined as the ratio of the axial flux of momentum to the axial flux of axial momentum times the radius of the rotating flow. The diameter of the vortex core is assumed to be given by the radial location of the maximum velocity component. In this configuration, the radial location of the maximum of v varies with z as illustrated in Fig. 3(c) for $z = 0$ and $z = -0.75$. It moves from the axis to the vertical boundary

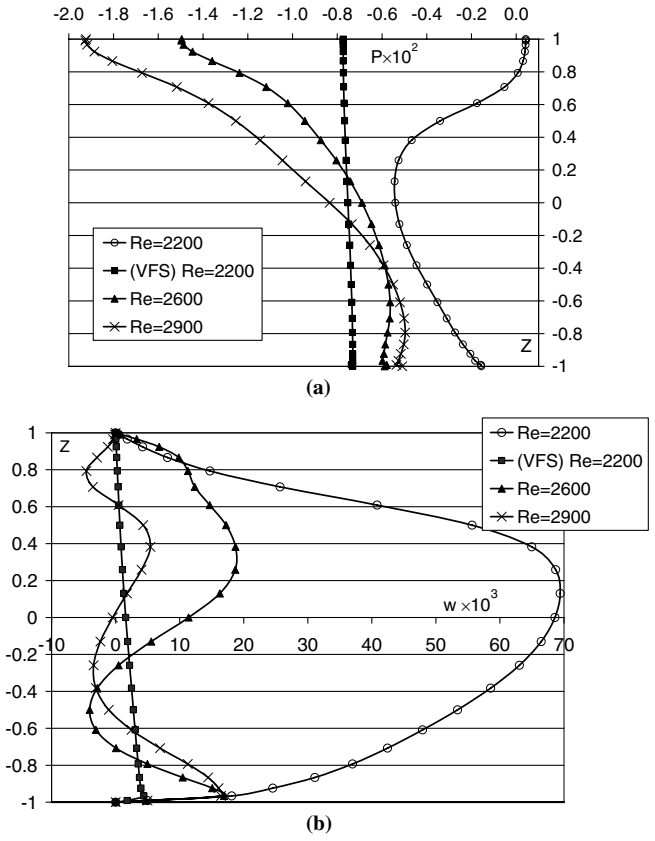

Fig. 4. Axial profiles of the pressure p (a) and the vertical velocity component w (b) at different Reynolds numbers. At $Re = 2200$, the container wall can be replaced by a vertical free-surface (VFS). The rotating disk is located at $z = -1$.

layer when the flow moves closer to the rotating disk. Then, the radial averaged position $r \approx 0.4$ ($r^* \approx 2R/3$) has been calculated over the height of the cavity and outside the vicinity of the stress-free and the rotating disk. As proposed by Spohn et al. (1998), we define a simplified swirl parameter S:

$$S(z) = 2 \times v(0.4, 0, z)/w(-1, 0, z),$$

where the axial velocity w is directly measured on the axis ($r = 0$), which provides a good estimate of the mean axial velocity in the jet. The quantity $2v^*(2R/3, 0, z^*)/R$ characterizes the angular velocity of the vortex in this part of the cavity (this is not, strictly speaking, the slope of v^* at the axis as in some other definitions of the swirl parameter).

6.2. Onset of vortex breakdown and evolution

In this section the Reynolds number is increased step-by-step from the base state at $Re = 2200$ up to $Re = 2950$. For all the Reynolds numbers considered in this section, the flow is steady and there is no evidence of three-dimensional effects. The energy E_k of all non-axisymmetric modes $k \neq 0$ remains close to the machine-zero and shows that no asymmetry effect is induced in the solution during the onset of the vortex breakdown. The three-dimensional streaklines of particles, analogous to dye visualizations in the experiments, were calculated for particles released close to the free-surface. All the particles introduced precisely on the centerline remained there, confirming the axisymmetry of the solution observed in Eulerian computations (Hourigan et al., 1995). The particles were released at six equidistant azimuthal positions close to the axis at a local radius $r = 0.025$ ($r^* \approx R/10$). At $Re = 2300$, no perturbation is visible along the axis and the swirl parameter S remains constant along the axis outside the two end wall regions. An increase in Re up to $Re = 2400$ causes the formation of a disturbance near the rotating disk in the form of a helical structure located at about $z = -0.5$ (Fig. 5(a)). This helical structure is steady and fixed in space and is caused by a divergence of the streamline, taking the particle further away from the axis. The swirl parameter, S, now increases as illustrated in Fig. 6. A local maximum of S occurs along the axis at about $z = -0.525$, mainly due to a decrease of the axial velocity w between the jet-like region and the boundary layer of the rotating disk, v remaining almost constant in the axial direction in this flow region (as illustrated in Fig. 5(c) at $Re = 2600$).

At $Re = 2500$, the helical structure has a more pronounced radial stretching. However, no stagnation point is observed on the axis despite the axial component of the velocity being very close to zero at this location ($w \approx 10^{-3}$). A slight increase in the Reynolds number to $Re = 2550$ leads to the occurrence of the first stagnation point $w = 0$, at $z = -0.5$, very close to the maximum of S observed in Fig. 6. However, no flow recirculation is observed downstream of this point. As shown in Fig. 4a, the adverse gradient pressure in the vortex core increases with rotation. At $Re = 2600$, the vertical component of the velocity reaches negative values after $\Omega t = 200$ (Fig. 4(b)). In Fig. 5(b) the particle streakline along the axis is shown for $Re = 2600$. The results reveal an axisymmetric bubble with two stagnation points along the centerline of the cylinder, one at the leading edge of the bubble, and another just slightly downstream. These two free internal stagnation points (located at $z \approx -0.27$ and $z \approx -0.70$) form a closed region of reversed axial flow (Fig. 5(c)). The intensities of the velocity components inside the bubble are weak, the maximum vertical velocity component being five times smaller inside the bubble than outside. As shown by the axial profile of the radial velocity (Fig. 5(c)), radial outflow is required upstream of the recirculation region which is succeeded by radial inflow in the wake of the bubble to satisfy mass conversation. The azimuthal velocity component almost vanishes inside the bubble and reaches its minimum at the center of the bubble at $z = -0.5$. Then, the fluid particles carrying azimuthal momentum are shifted to larger radii. The bubble is centered on $z = -0.5$, close to the location of the maximum of S observed at $Re = 2400$ (Fig. 6) and consequently at the same location as the helical disturbance (Fig. 5(a)). This observation seems to confirm that the axisymmetric bubble

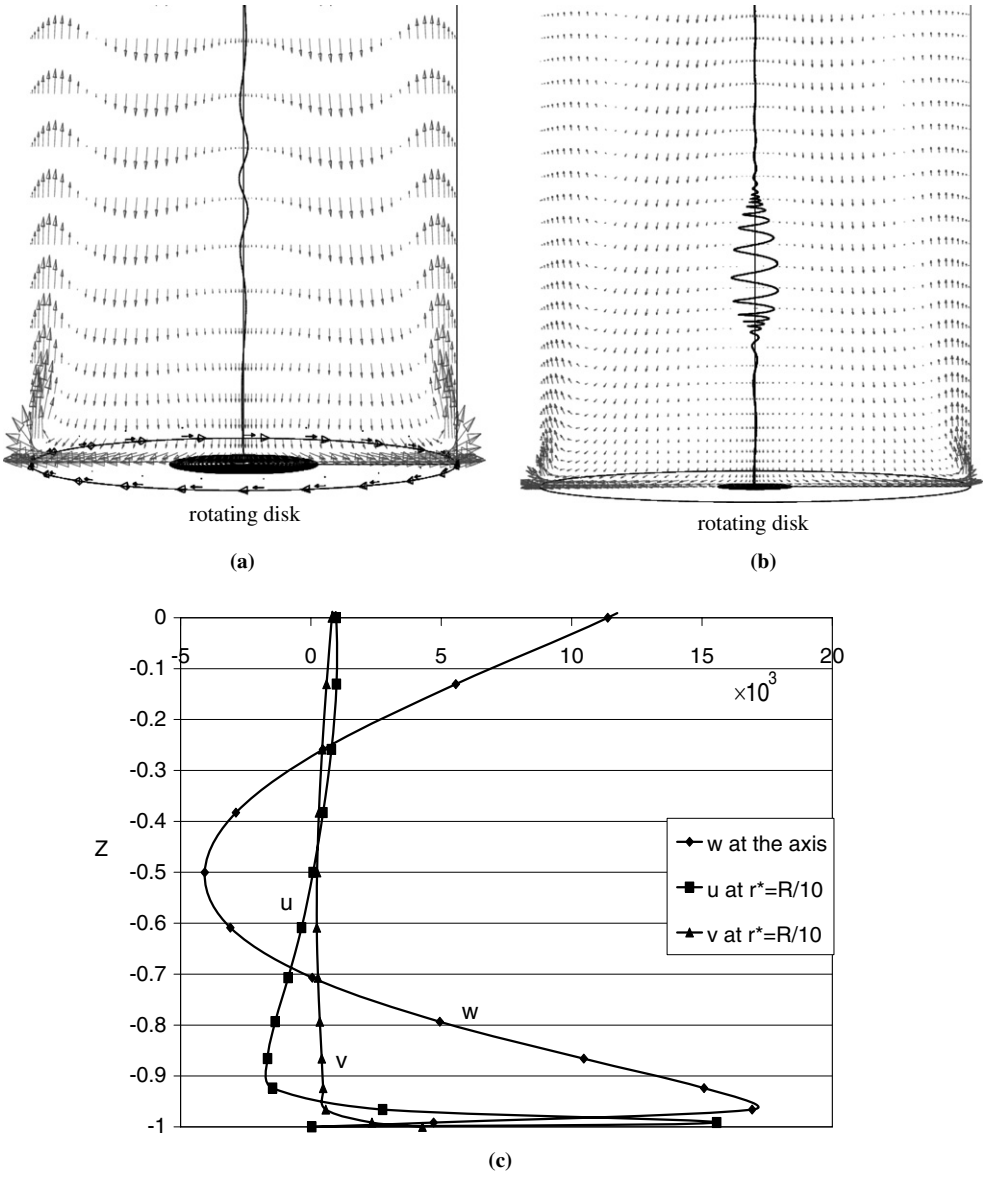

Fig. 5. Onset of vortex breakdown. Flow field with streaklines of particles released at the top of the cavity (close to the free surface) and around the axis. In grey, velocity field projected in the meridional plane (r, 0, $-1 \leqslant z \leqslant 0$) (a) and (b). At $Re = 2400$ (a), disturbance in the form of a helical structure near the rotating disk. At $Re = 2600$ (b), axisymmetric bubble related to vortex breakdown. (c) Axial profiles of the three velocity components at $Re = 2600$ showing a recirculation flow region.

breakdown evolves from a single helix which undergoes radial stretching due to the increase in rotation and then forms a recirculating flow region located between two stagnation points, as observed experimentally. In the present results, the local maximum of S occurs between $Re = 2300$ and $Re = 2400$ but there is no evidence of the continuous nature of the vortex breakdown process by increasing Reynolds number. The helix gets replaced by a bubble for a swirl parameter in the range, $0.38 < S \leqslant 0.75$. These values of the swirl parameter S are in good agreement with the results given in the literature for confined vortex flows with vortex breakdown. For example, studies in a vortex tube with radial inlet guidevanes (Faler and Leibovich, 1977; Escudier, 1988), give a value of S for vortex breakdown in the same range $0.4 \leqslant S \leqslant 0.7$.

By increasing continuously the rotation rate to $Re = 2850$, the bubble grows and has a more pronounced radial and axial stretching. A second breakdown occurs upstream of the first one at $Re = 2900$. This second recirculation zone is originally smaller and occurs just below the free-surface (Fig. 7(a)). This flow configuration is unstable and the second bubble that grows rapidly in time finally merges to the free-surface (Fig. 7(c)). The axial profile of the vertical component of the velocity (Fig. 4(b)) shows that the flow intensity is similar in both bubbles. Contrary to the bubble growth at lower Reynolds numbers ($2600 \leqslant Re \leqslant 2850$), the lower bubble expands more in the axial direction than in the radial direction. By increasing the Reynolds number, this tendency is amplified and the attached bubble grows along the axis too. Finally, at

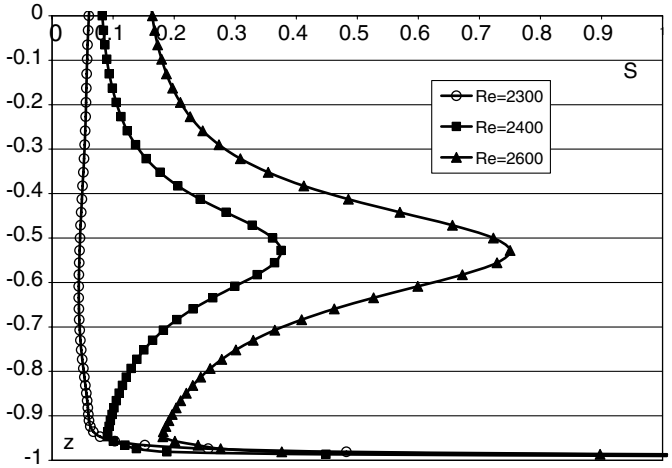

Fig. 6. Axial profiles of the swirl parameter S along the axis in the half-lower part of the cavity ($-1 \leqslant z \leqslant 0$): at $Re = 2300$ (no breakdown), $Re = 2400$ (helical disturbance) and $Re = 2600$ (bubble vortex breakdown).

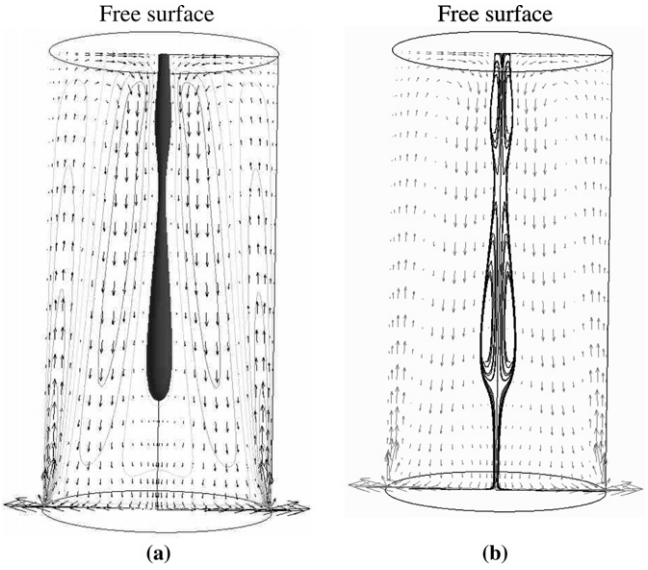

Fig. 8. Elongated bubble attached to the free-surface at $Re = 2950$. (a) Vector velocity field and isolines of $w = \pm 0.05$ in the meridional plane. The vortex breakdown is characterized by the isosurface $w = 0$. (b) Velocity vector field and streaklines emphasizing two separated recirculation flows within the vortex breakdown.

$Re = 2950$, the two bubbles merge and form an elongated axisymmetric vortex breakdown region which is attached to the free-surface (Fig. 8(a)). Streaklines calculated for particles released around the axis and close to the free-surface (Fig. 8(b)) show the internal structure of the vortex breakdown after the merging and demonstrate that two structures persist in the merged bubble.

6.3. Onset of unsteadiness

The basic state remains stable up to $Re = 2950$. Starting from $Re = 2950$, the transition from a steady to a multi-frequency regime is obtained via successive bifurcations in a short range of Reynolds numbers [2950, 3150]. This may be explained by the destabilizing effect of the free-surface on the confined flow, as previously observed experimentally in large aspect ratio cavities by Spohn et al. (1993). The time histories of the vertical velocity component recorded at the centre of the cavity, together with the logarithm of the Fourier spectrum, are shown in Fig. 9 at different Reynolds numbers, from the first oscillatory state at $Re = 3000$ to the multi-frequency regime at $Re = 3150$ with more than five different frequencies.

The basic state undergoes a symmetry breaking bifurcation at $Re = 3000$ to an azimuthal mode with wavenumber $k = 3$ (Fig. 10(a)). Due to prohibitive three-dimensional computational costs, the transition point has not been resolved more precisely than within the Re range [2950,

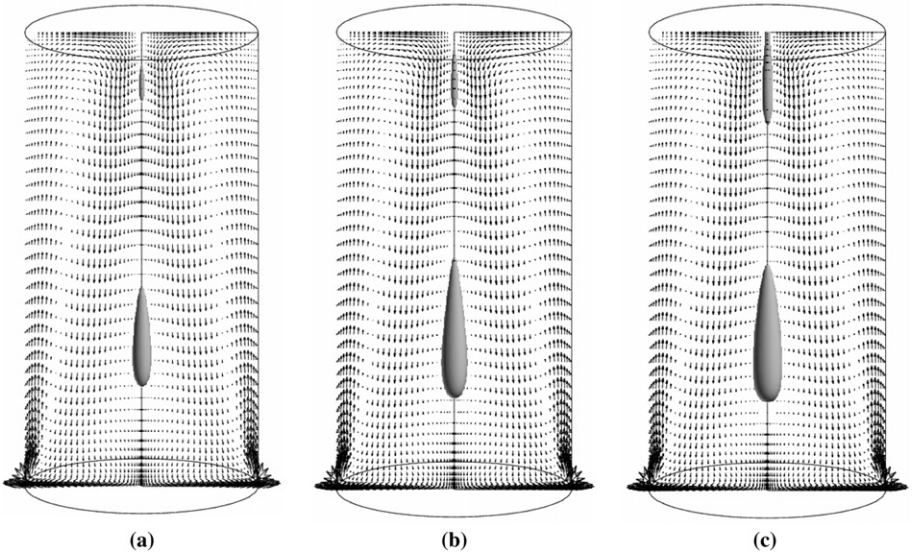

Fig. 7. Attachment of the bubble to the free-surface at $Re = 2900$. Time evolution of the bubbles positions: (a) $\Omega t = 1500$, (b) $\Omega t = 1800$, (c) $\Omega t = 2100$ (final steady state). Velocity vector field and isosurface of $w = 0$, in the meridional plane (r, 0, z).

3000]. The transition probably occurs through a supercritical Hopf bifurcation as suggested by the general behaviour of the flow response in the vicinity of the critical Reynolds number that is the slow exponential convergence to the stationary state below the transition and the lack of a hysteretic cycle. This result is also supported by recent numerical and experimental studies in a $\Gamma = 2$-cavity by Hirsa et al. (2002) and Lopez et al. (2004). As it is shown in Fig. 9, this $k = 3$ mode is a rotating wave with a small precession frequency $\sigma = 0.05$ (where $\sigma = 2\pi f \Omega^{-1}$) twenty times smaller than the rotation frequency ($\sigma_{rot} = 1$). The spatial structure of the $k = 3$ mode is clearly visible in Fig. 10(a). This figure shows the isosurface of the radial velocity component for $u/\Omega R = 5 \times 10^{-2}$. The isocontours of the vertical component of the velocity in Fig. 10(c) show that the $k = 3$ rotating wave is dominant in the vertical wall boundary layer just below the free-surface at about $z = 0.75$. Rolls are convected in spirals by the main flow to the top free-surface (Fig. 10(a)) and reach the core region where they combine into a helical vortex pattern before vanishing in the vicinity

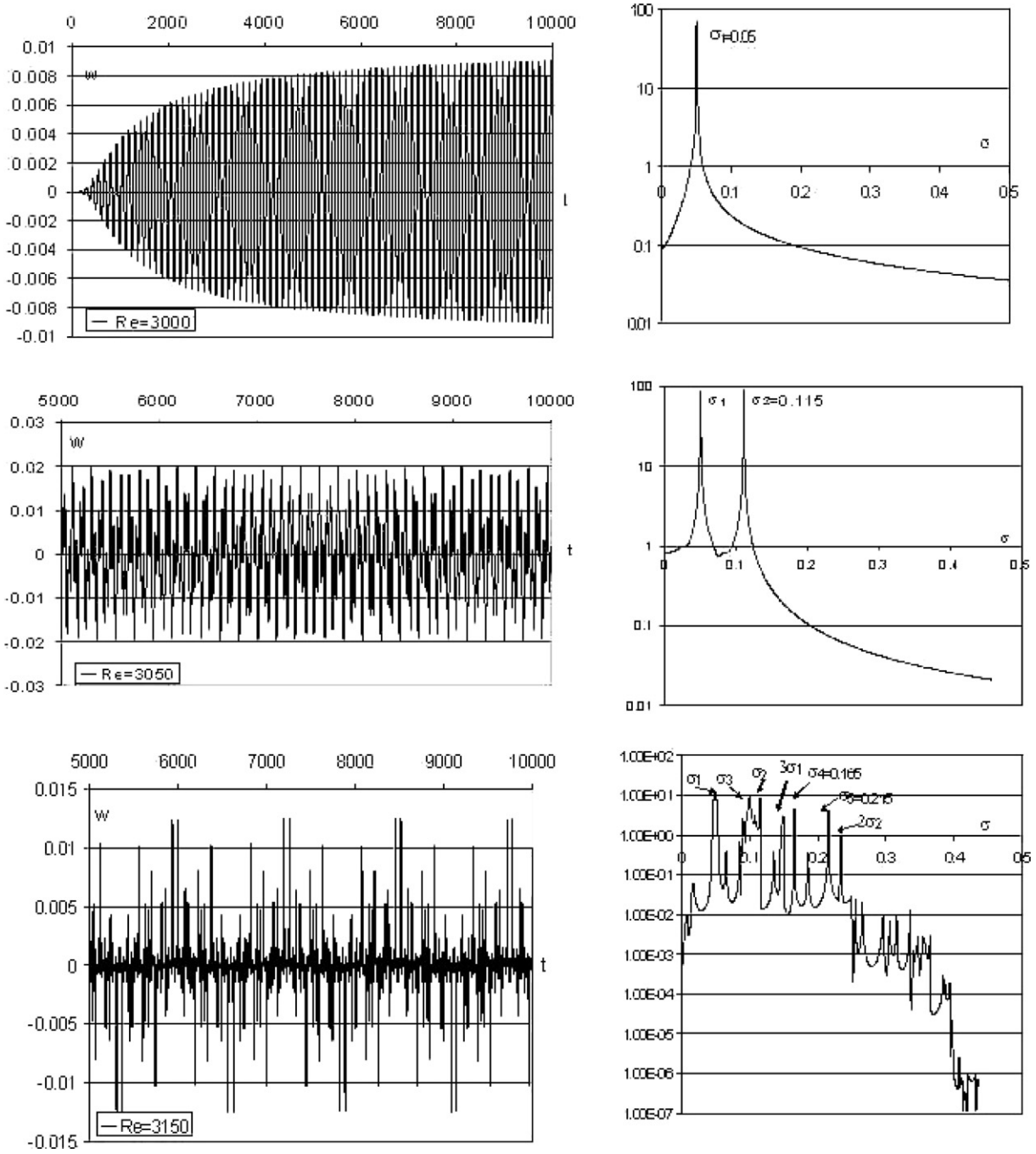

Fig. 9. Time histories of the vertical velocity component w recorded at the centre of the cavity together with the logarithm of the Fourier spectrum. Different Reynolds numbers are shown ($Re = 3000$, 3050 and 3150) in order to characterize the transition from a steady state to a multi-frequency regime.

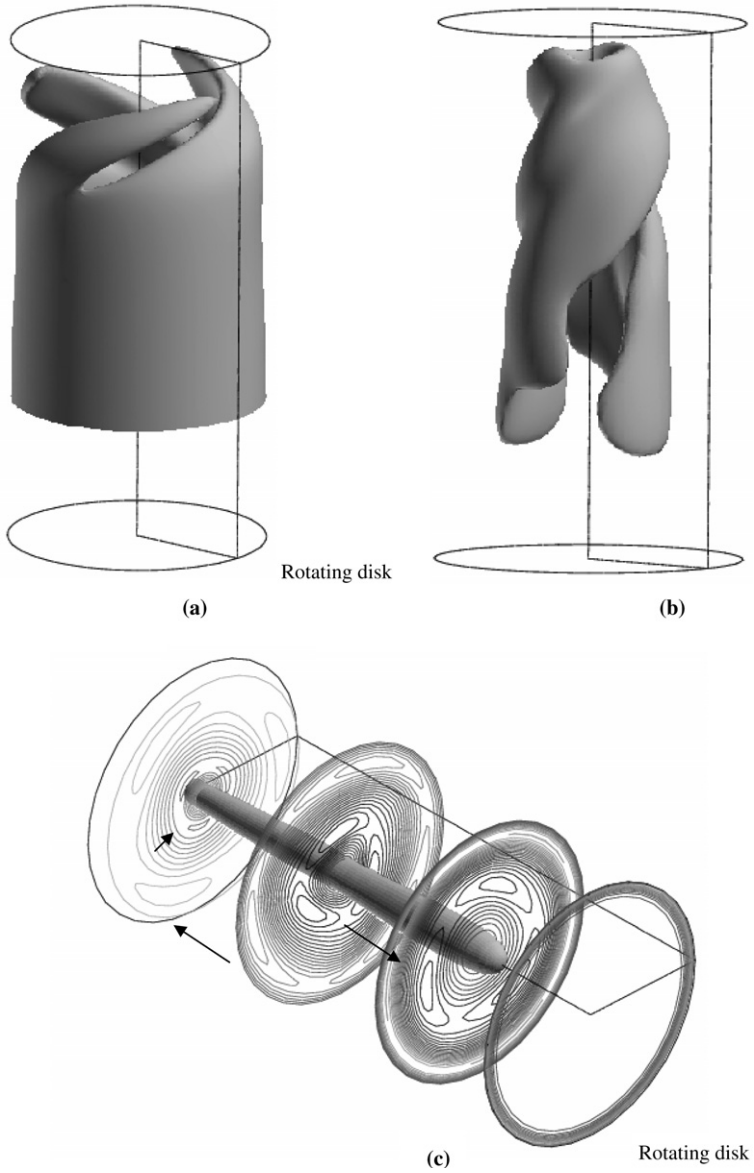

Fig. 10. Vortex breakdown attached to the free surface and three-dimensional modes of instability. (a) Spatial structure related to the $k = 3$ mode of the Stewartson layer at $Re = 3000$ (isosurface of $w = 0.031$). (b) Double helical structure related to the $k = 2$ mode in the core flow at $Re = 3080$ (isosurface of $w = -0.036$). (c) Isosurface $w = 0$ and isolines of $w = \pm 0.036$ at four different axial coordinates along the axis at $Re = 3000$. The black arrows show the travelling direction of the instability structures within the main flow.

of the rotating disk (Fig. 10(c)). At this rotation speed, the vortex breakdown is still composed of one elongated recirculation bubble attached to the free-surface (Fig. 10(c)). This bubble remains axisymmetric and it is not affected by the travelling structures related to the 3D mode of instability.

At about $Re = 3050$ the $k = 3$ rotating wave becomes unstable to a $k = 1$ mode. When the $k = 1$ mode saturates at $\Omega t = 3500$, the elongated vortex breakdown attached to the free-surface rapidly mutates into a "S-shape" (Fig. 11(a)) as noted in Serre and Bontoux (2002). The vortex breakdown starts precessing around the axis (Fig. 11) at a rotation frequency $\sigma = 0.115$, equal to about twice the base frequency ($\sigma = 0.05$) related to the $k = 3$-wave. Such observation indicates that the $k = 1$ mode is responsible for the precessing motion of the bubble. In agreement with the visualizations of Billant et al. (1998) in a swirling jet, the vortex breakdown precesses in the same direction as the main upstream flow forced by the rotating disk. The downstream stagnation point is now off the cylinder axis. At $\Omega t = 4000$, the recirculation flow region breaks into two parts as shown in Fig. 11(b). The upper part is more elongated and remains attached to the free-surface while the lower part, of smaller size, is now off the cylinder axis. The $k = 3$ and $k = 1$ modes have incommensurate "precession frequencies" (Fig. 9) and the resultant state is now a modulated rotating wave whose structure is not time invariant in any rotating frame. This observation suggests

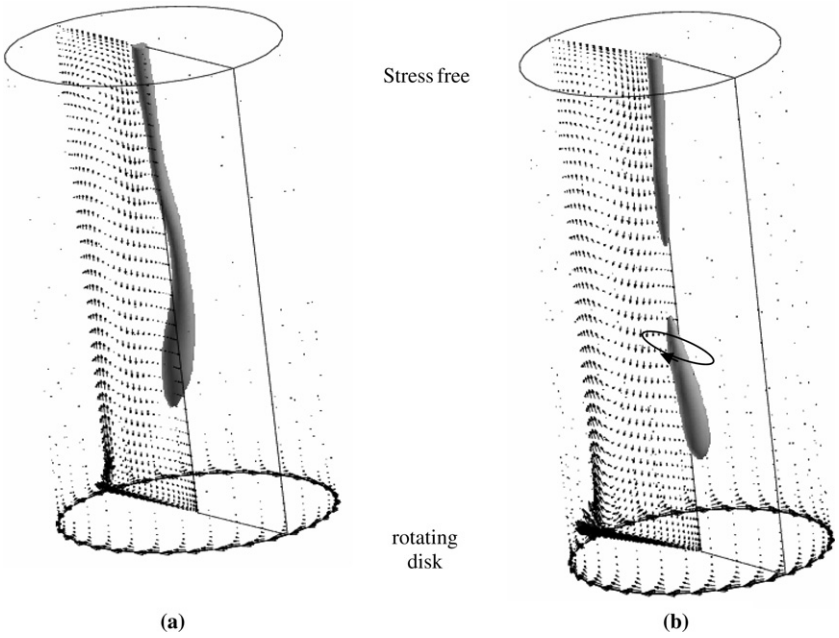

Fig. 11. Time evolution of the 3D vortex breakdown at $Re = 3050$. (a) $\Omega t = 3500$, transition from an elongated axisymmetric bubble to a "S-shaped" vortex breakdown. (b) Final state at $\Omega t = 5000$, showing a vortex breakdown broken into two asymmetric bubbles precessing around the axis (the black arrow on the circle indicates the precession direction). Velocity vector field in the meridional plane (r, π, z) and along the vertical wall.

that the instability of the $k = 3$ rotating wave is via a Neimark–Sacker bifurcation as obtained in the configuration with rigid cover by Marques and Lopez (2001) and Serre and Bontoux (2002). This result shows a different scenario to that observed in a smaller $\Gamma = 2$-cavity by Young et al. (1995) and Lopez et al. (2004) where the instability of the rotating wave is via a period doubling bifurcation. At a slightly higher Reynolds number, $Re = 3080$, a third mode of instability grows which corresponds to a $k = 2$ wave of frequency $\sigma = 0.095$. This mode is characterized by a double helical structure spatially developing in the axial direction and also rotating in the same azimuthal direction as the upstream flow (Fig. 10(b)).

The spatial structures of the axisymmetric flow as well as the instability modes are shown separately (Fig. 12). By increasing the rotation rate, almost the entire flow region becomes three-dimensional. Only the lower half of the vertical boundary layer, where the Ekman boundary layer on the rotating disk is turned into the interior by the stationary cylinder, is dominated by the $k = 0$ mode (Fig. 12(a)). The low intensity of the time-averaged modal energies E_3, E_1 and E_2 compared to E_0 (typically a ratio 10^4) shows that the level of distortion to the axisymmetric flow caused by the two successive Neimark–Sacker bifurcations is relatively small. Both $k = 1$ and $k = 2$ modes are more concentrated in the vortex core region (Fig. 12(b) and (c)). Their maxima are mainly located in the vortex breakdown flow region, and they extend (for the $k = 1$ mode only) slightly lower within the wake of the vortex bubbles. In this configuration, the vortex breakdown merges with the free-surface and there is no upstream flow as occurs in the case with a rigid cover, where the flow rebounds from its collision at the axis on the stationary disk. Therefore, the $k = 1$ mode of instability cannot be associated with a jet-like instability of the upstream flow (developing between the steady rigid cover and the bubble), as recently suggested in Serre and Bontoux (2002). The mechanisms related to $k = 1$ and $k = 2$ modes certainly require further investigations, involving theoretical analysis of the stability of the velocity profiles along the axis. In contrast, the mechanism related to the $k = 3$ mode is easier to identify, the modal energy E_3 being concentrated within the vertical boundary layer. This mode can therefore be related to the instability of the wall-jet flow produced near the cylindrical wall as previously suggested in the rigid cover configuration in Blackburn (2002).

The subsequent bifurcations are more complicated to discern because of their occurrence over a short range of Reynolds numbers and it would be to time consuming to specify them all. At $Re = 3150$, the time signal is characterized by more than five frequencies and harmonics exhibiting a complex time behaviour (Fig. 9). The vortex breakdown structure is now re-attached in a single elongated structure entirely three-dimensional. The topology of the vortex breakdown is now more irregular (Fig. 13) than at lower Reynolds numbers. The structure of the recirculation flow region exhibits concave and convex surfaces delimited by the $w = 0$-isosurface. The bubble then expands over 3/4 of the cavity height and still precesses around the cylinder axis in the same direction as the main flow (i.e., in the direction of the rotating disk). The topology of the lowest part of the vortex breakdown shows some similar characteristics with that previously observed in the rigid cover case at much higher Reynolds number

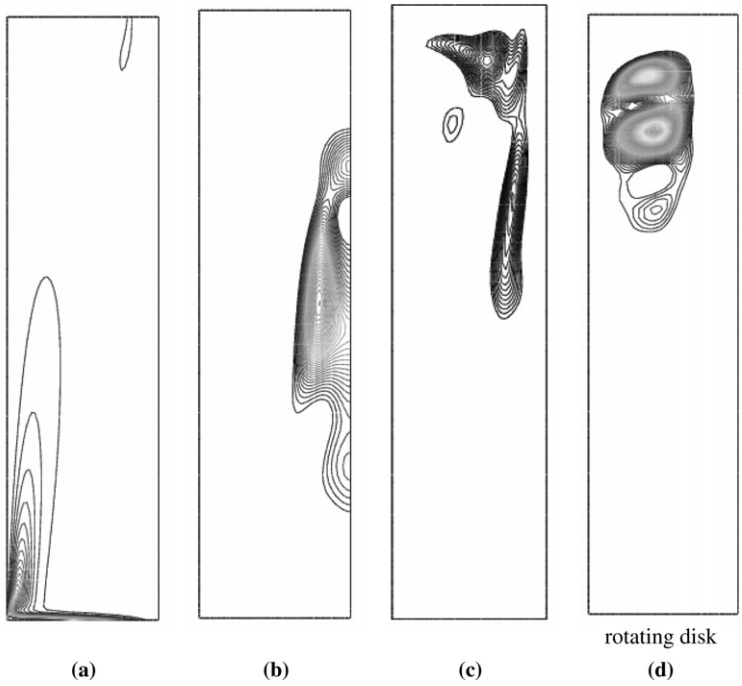

Fig. 12. Time-averaged isolines of the energies E_k in the meridional plane (r, 0, z) emphasizing the location of the dominant modes at $Re = 3080$. (a) $k = 0$ mode, $[0\,;10^{-2}]$. (b) $k = 1$ mode, $[0;1.5\times10^{-5}]$. (c) $k = 2$ mode, $[0;2\times10^{-6}]$. (d) $k = 3$ mode, $[0;4\times10^{-6}]$. The values in the brackets indicate the respective magnitude of the variation of the different energy modes, E_0, E_1, E_2 and E_3, respectively. The cavity axis is on the right side and the free-surface is at the top.

$Re = 5500$ and designated of "spiral type" (Serre and Bontoux, 2002).

The temporal evolution of the flow vortices at $Re = 3150$ is illustrated by 6 snapshots at different times instants in the meridional plane (r, 0, z) and close to the free-surface (Fig. 14). The symmetry around the axis is now completely broken and the jet-shear layer instability ($k = 3$) is now so intense that it involves sometimes a vertical boundary layer separation (at Ωt_0 and $\Omega t_0 + 2000$, for example). Large secondary vortices occur just below the free-surface in the return region of the vertical sidewall layer. When re-attaching the wall cylinder, the flow compresses these vortices on the free-surface which cannot be deformed, reinforcing, in the process, the intensity of these vortices. In the breakdown recirculation region, the velocity field displays an intense tilting of the whole reverse flow around the cylinder axis related to the $k = 1$ mode of instability. Consequently, the vortex breakdown is now eccentric, involving at the free-surface a motion of the outflow region ($u \geqslant 0$) around the axis as further described in Section 7.

7. Discussion

7.1. Comparison with the literature

Our results can be compared with experimental studies of Spohn et al. (1993, 1998) and with theoretical and numerical results of Brøns et al. (2001). All these results have been summarized in Table 2 and show relatively good agreement. Except for the recent paper of Lopez et al. (2004) in $\Gamma = 2$ and $\Gamma = 0.25$ cavities, the numerical results have until now been limited to axisymmetric simulations.

Concerning the topology of the vortex breakdown, the present results agree quite well with the 2D numerical results of Brøns et al. (2001, see Table 2). Indeed, both studies show a detached bubble for Reynolds numbers in the range [2600, 2900], evolving into two bubbles at higher rotation, one of which being attached to the free-surface. In the experiments, the recirculation bubble occurs at a slightly lower Reynolds number ($Re = 2500$) than in the two previous studies but at the same location near the rotating disk. The flow configuration with two detached bubbles observed by Spohn et al. (1993) in the narrow range of Reynolds numbers, $2900 \leqslant Re \leqslant 3000$, has been shown to be unstable in our study. Two detached bubbles have only been observed during a transient time at $Re = 2900$, before the upper bubble merges with the free-surface (Fig. 7). Moreover, the very elongated vortex breakdown is formed on the free-surface at a lower Reynolds number ($Re = 2950$, Fig. 8) than observed in experiments ($Re \approx 3150$).

Concerning the temporal regimes, information is missing in the literature and we can only compare the transition to unsteadiness. The agreement between numerical simulations and experiments is not as good as for the flow with a rigid cover (see Serre and Bontoux, 2002). Indeed, as for large aspect-ratio cavities, the transition is expected to be related to a three-dimensional mode of instability (Escudier, 1984), Brøns et al. (2001) cannot accurately capture

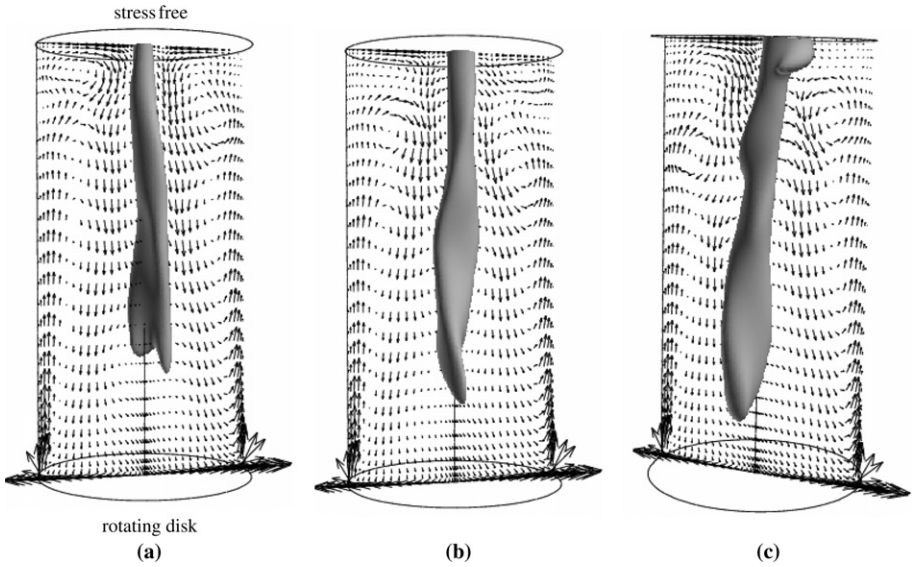

Fig. 13. Three-dimensional time-dependent vortex breakdown attached to the free-surface at high rotation rate $Re = 3150$. Isosurface $w = 0$ and velocity vector field. (a) $\Omega t = 3100$, (b) $\Omega t = 3200$ and (c) $\Omega t = 3300$. The structure rotates in the direction of the disk.

the critical Reynolds number: they found an unsteady regime at $Re = 3659$, that is much larger than the one found in the present study, $Re \approx 3000$ as well as in the experiments of Spohn et al. (1993), $Re \approx 2800$. Our results slightly overestimate the experimental critical Reynolds number, which is not really surprising and can be explained both by the free-surface modelling in the numerical approach and by the experimental difficulties in accurately measuring the transition. Indeed, the modelling of the free-surface by a flat stress-free is a relatively hard constraint. Particularly, the absence of oscillations at the surface, that are supposed to play a crucial role in the transition to oscillatory flows, could explain this delay in the transition. On the experimental side, the free-surface makes the configuration very unstable and sensitive to external noise which can bring about instability earlier. Moreover, as explained by Spohn et al. (1993), the identification of unsteady states becomes tricky for $\Gamma \geqslant 3$ because different mechanisms lead to boundary layers instabilities, vortex breakdown oscillations or wake oscillations of the breakdown bubble. Therefore, experimental identification of unsteady flow states in a large aspect ratio cylinder may be not very accurate (Spohn et al., 1993, 1998).

7.2. Attachment of the bubble to the free-surface

The existence of a cylindrical vortex core upstream of the breakdown is usually included in the classical theories based on idealized models of the vortex flows (Benjamin, 1962). Consequently, the attachment of the bubble to the free-surface could seem unexpected.

Its mechanism is related to two characteristics of the flow associated with the presence of a free-surface. The first is the absence of a boundary layer on the free-surface due to the slip condition. The second one is the weak intensity of the Ekman pumping at small radii (relatively to the rigid cover case), due to the conservation of the angular momentum along the free-surface. That involves a weak axial outflow coming from the free-surface along the axis. A consequence of that is the increase of the swirl parameter S (compared to the rigid cover case) which promotes the occurrence of vortex breakdown in this flow region.

Radial profiles of the angular momentum rv and of the radial component of the velocity u measured on the free-surface are shown in Fig. 15. According to the theoretical analysis of Rogers and Lance (1960), the pumping due to the rotating disk is proportional to the difference between the angular velocity of the disk and the angular velocity of the fluid. Now, as the fluid is supposed to conserve its angular momentum during the radial motion, its angular velocity has to increase when the radius decreases. Then, following the Ekman pumping theory for an infinite disk, the radial inward progression of the fluid along the free-surface (only caused by the Ekman pumping) should decrease with radius and also stop at a radius r_0 where the angular velocity reaches Ωr_0. Here, the angular velocity never reaches r_0 (therefore, the radial inward motion is never stopped) and, due to radial confinement, the angular momentum is only conserved ($rv \approx 0.048$) over a flow region at about mid-radius around $r = 0.2$ (Fig. 15(a)). Indeed, due to the zero-velocity boundary conditions at the axis and at the wall, the angular momentum must vanish at these two locations and then by continuity cannot remain constant over the entire cavity radius. Moreover, the angular momentum is strongly influenced at large radii by the turning flow coming from the vertical sidewall layer, which strongly modifies the flow along the free-surface. The difference between the angular momentum on the rotating disk and the angular momentum of the fluid on the free-surface reduces with radius and almost vanishes

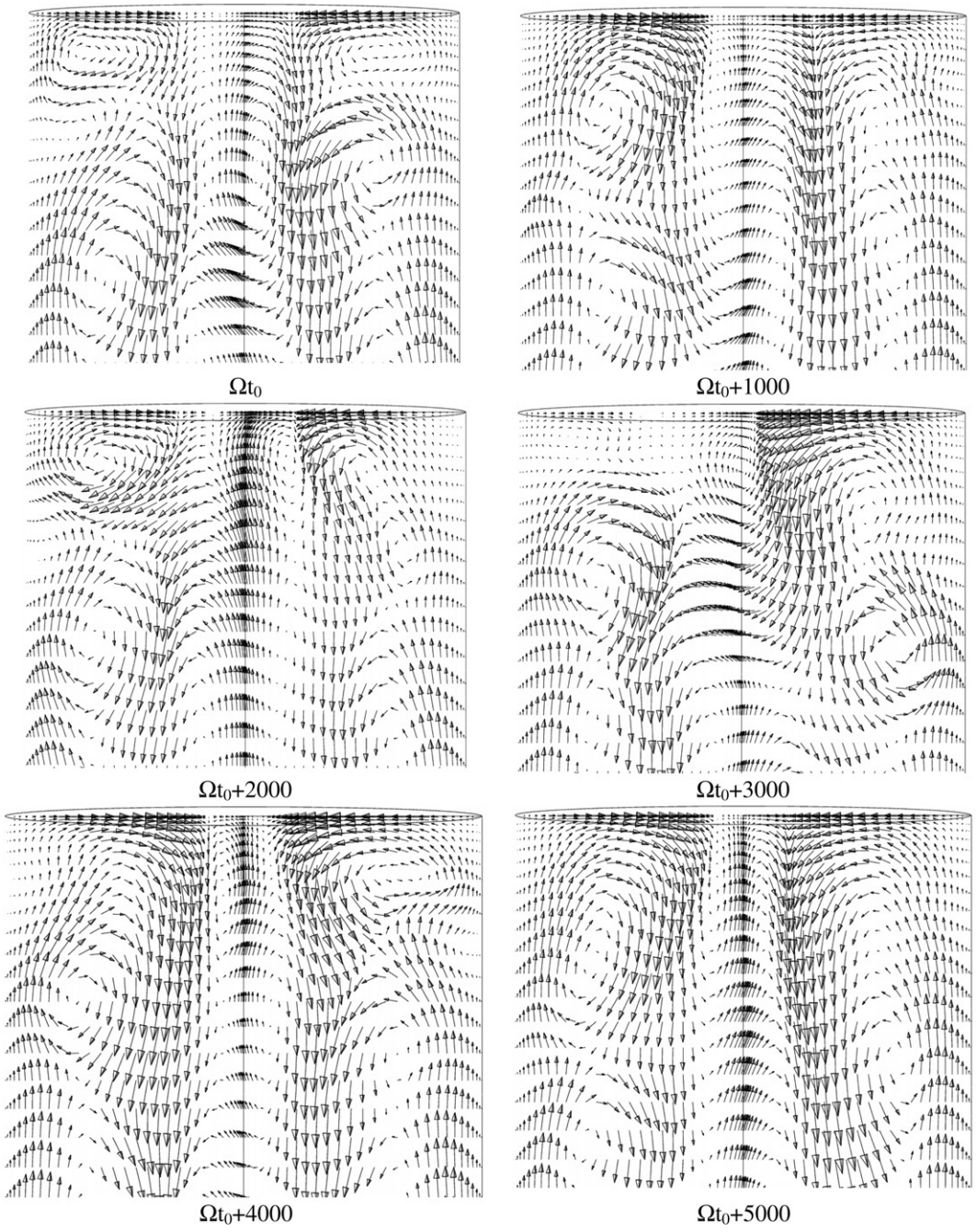

Fig. 14. Projected velocity vector field in the meridional plane (r, 0, z) and in the vicinity of the free-surface at $Re = 3150$ showing the dynamics of the vortices. Sequence of six time instants. The time step between each sequence is equal to $\Omega t = 1000$.

in the near-axis region ($r^* < R/10$). As a consequence, outside the turning flow region, the intensity of the radial motion along the free-surface decreases with the radius and becomes very weak around the axis as shown in Fig. 15(b). At $Re = 2550$, the radial component of the velocity decreases from $u/\Omega R = -2 \cdot 10^{-2}$ to $u/\Omega R \leqslant -5 \times 10^{-3}$ between $r = 0.14$ and $r = 0$. When the bubble merges with the free-surface at $Re = 2900$, a small $u \approx 0$ – central fluid cylinder of radius $r = 0.02$ ($r^* \approx R/20$) is excluded, replacing the usual upstream stagnation point with a disk of stagnation. From $Re = 2925$ and at larger Reynolds numbers, the flow intensifies within the vortex breakdown and becomes larger than the natural inflow along the free-surface due to the Ekman pumping. Then, the disk of stagnation becomes an outflow region ($u > 0$) bounded by a circle of stagnation $u = 0$ of radius rapidly increasing with Re:$r = 0.065$ at $Re = 2925$ and $r = 0.1$ at $Re = 2950$ (Fig. 15(b)).

Slightly above the transition to unsteadiness ($Re = 3050$), the $k = 1$ mode seems to affect mainly the lower-half part of the recirculating flow region (Fig. 11) which is consistent with the location of the maximum intensity of the

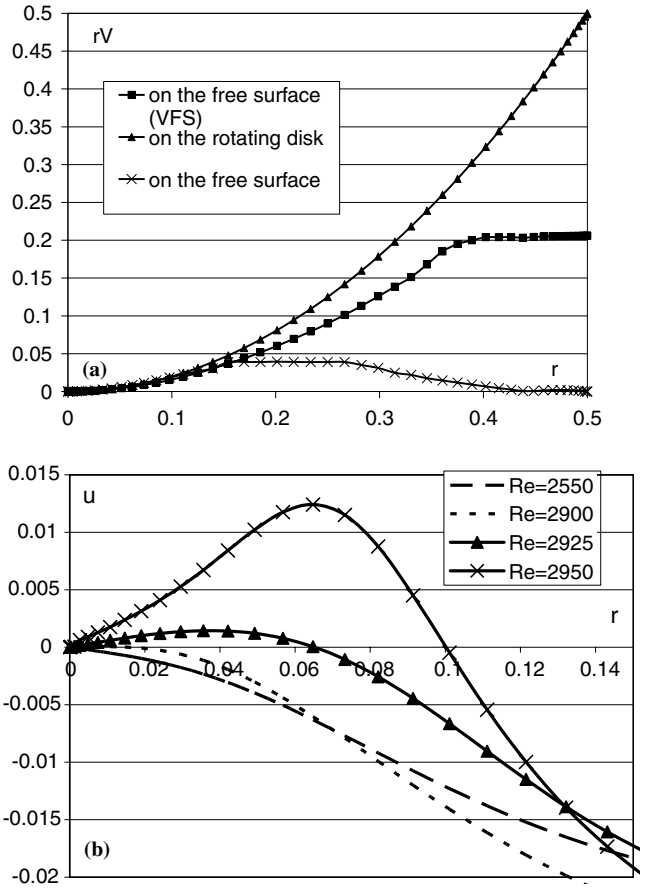

Fig. 15. (a) Radial profiles of the angular momentum rv at $Re = 2550$ measured on the rotating disk and on the top free-surface in two configurations: with a vertical solid wall and with a vertical slip-surface (VSF). (b) Radial profiles of u on the free surface in the near-axis region at different Reynolds numbers.

$k = 1$ mode (Fig. 12(b)). Incidentally, the stagnation circle at the free-surface remains almost at rest around the axis as in the steady regime. By increasing the rotation up to $Re \approx 3150$, the vortex breakdown is now moving on the free-surface. Due to the intense tilting of the reverse flow provoked by the $k = 1$ mode of instability the shape of the vortex breakdown base at the free-surface becomes much more irregular. It evolves from a circular $u = 0$-line at $Re = 2925$ to non-convex shapes illustrated in Fig. 16 by isolines of $u \geqslant 0$ shown at 6 different time instants. These outflow regions rotate in the same direction as the rotating disk and eventually move away from the rotation axis (for example in Fig. 16 at $\Omega\, t_0 + 1300$). Within these flow regions, the distribution of radial velocity is non-homogeneous and the location and the intensity of the maximum change in time.

7.3. Comparison with the configuration with rigid cover

The results show that changing upstream condition substantially modifies both the flow and the vortex breakdown structure in the cylinder.

- The onset of a periodic motion ($Re \approx 3000$) is found at a much lower Reynolds number than in the rigid cover case ($Re \approx 3500$ in Serre and Bontoux, 2002). The existence of a free-surface intuitively has a destabilizing effect which promotes the onset of unsteadiness. Nevertheless, the instability frequencies remain of the same order in both configurations, and about fifteen to twenty times smaller than the rotation frequency. Moreover, the first bifurcation remains of Hopf type and the successive bifurcations of Neimark–Sacker type.
- Vortex breakdown keeps the same topology in both configurations: of bubble type at the onset, it switches to a spiral-like type in unsteady regimes that precesses around the cylinder axis in the same direction than the rotating disk. The precession frequencies are very close in both configurations and equal to one tenth of the rotation frequency. One of the most striking differences between the both configurations is the occurrence of a breakdown bubble attached to the free-surface. Bubbles attached to the rigid cover are never observed. Details on this phenomenon have been previously discussed in Section 7.2. The first recirculation bubble occurs here at much lower Reynolds number ($Re \approx 2600$) than in the case with rigid cover ($Re \approx 3500$) and consequently can be observed in steady regime in spite of the large aspect ratio. That may be explained by the removal of the stationary disk boundary layer. The radial profiles of w are shown in Fig. 17, in the boundary layer of the rigid cover (grey line), of the rotating disk (black line) and along the free-surface (dashed line). First, the deficit of axial flow rate between the two container extremities is changed between the two configurations. This deficit is provoked by the axial in- and out-flows which takes place over the whole boundary layer on the rotating disk while it is more concentrated around the rotation axis on the rigid cover and on the free-surface. On the free-surface, the axial flow slightly decreases around the axis and becomes weaker at small radii than in the rigid cover case, increasing the deficit of axial flow between the two configurations. This deficit of axial flow rate is related to the adverse pressure gradient because it must be balanced inside the core region by an adverse pressure gradient causing a radially-outwards flow. The adverse pressure gradient along the container axis is therefore modified. The second point concerns the magnitude of the axial outflow around the axis which is about four times weaker than in the rigid cover case (Fig. 17), involving an increase of the swirl parameter, the value of the azimuthal component of the velocity remaining almost the same.

7.4. Case of a cylinder with a vertical slip-surface

Many experiments on delta wings and tubes (cf, e.g., the review article in Lucca-Negreo and O'Doherty, 2001) demonstrated that changing axial pressure gradient in the far-field have profound effects on vortex breakdown. For

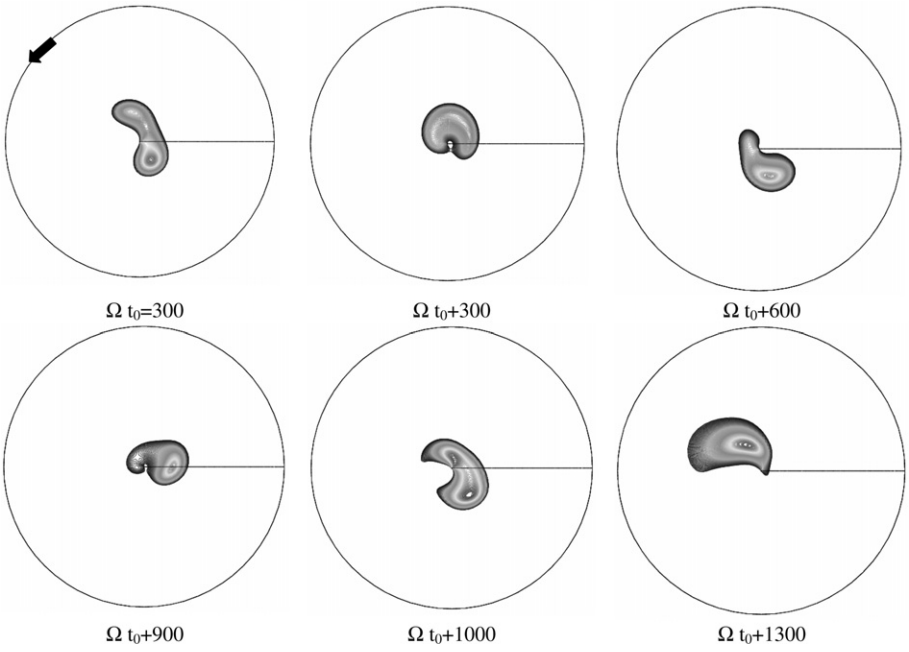

Fig. 16. Attachment of the vortex breakdown at the free surface at $Re = 3150$. Sequence of images at 6 different times of the radial velocity ($u \geqslant 0$). Isolines showing the outflow regions and the move of the vortex on the free-surface. The time step between each picture is equal to $\Omega t = 300$. The black arrow shows the rotation direction of the bottom rotating disk.

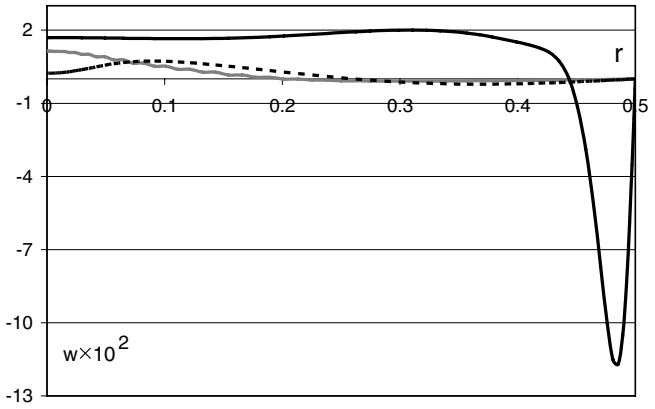

Fig. 17. Radial profiles of the axial component of the velocity w showing the out- and in-flows within the different radial boundary layers at $Re = 2000$: rotating disc layer (black), fixed disk (grey) and free-surface (dashed).

example, by prescribing a far-field pressure gradient on the lateral boundary of their computational domain Krause (1990) successfully initiates vortex breakdown and is further able to govern its mode selection. Here, in order to handle the flow and change the pressure distribution in the cavity, the container wall is replaced by a vertical slip-surface imposing no tangential stress $\partial w^*/\partial r^* = 0$ and $\partial v^*/\partial r^* - v^*/r^* = 0$ at r^*.

The flow obtained at $Re = 1500$ is shown in Fig. 3(b). The only wall is now the bottom rotating disk. Without any tangential stress, no boundary layer is formed along the vertical slip-surface. The flow issued from the Ekman layer swirls along the vertical slip-surface but remains parallel to it, in contrast to the configuration with a vertical wall. With no stress, the swirling fluid conserves its momentum along the vertical slip-surface longer than along the vertical wall. Consequently, the magnitudes of the both non-zero components of the velocity are much larger here than previously, as shown in Fig. 18 by the axial profiles of the azimuthal and axial velocity components measured at $r = 0.49$. Therefore, when the flow impacts on the top free-surface at $z = 1$, the angular momentum of the fluid along the free-surface is much larger than in the configuration with a vertical wall as shown in Fig. 15(a). As there is here no $v = 0$-condition at the slip-surface, the angular momentum is constant at the largest radii, $0.35 \leqslant r \leqslant 0.5$ ($rv = 0.2$, i.e. more than 10 times larger than the constant value obtained with a wall) before decreasing to zero on the axis. Consequently, the difference between the angular momentum on the rotating disk and the angular momentum of the fluid along the free-surface is globally much smaller here than with a vertical wall that limits the intensity of the Ekman pumping (following the theoretical analysis of Rogers and Lance, 1960). More precisely, an efficient Ekman pumping is limited at large radii ($0.35 \leqslant r \leqslant 0.5$) where the difference in the angular momenta is the largest (Fig. 15(a)). This result is consistent with the flow picture of Fig. 3(b). About the pressure, the diverging tube formed by the vertical boundary layer in the cavity with wall (Fig. 3(a)) is removed involving some changes in the pressure distribution, both in the far-field and along the cylinder axis. Along the vertical slip surface, the pressure gradient is larger over the entire height of the cavity except in a small region close to the rotating disk. Nevertheless, the most striking difference with the configuration with a vertical wall concerns the adverse pressure

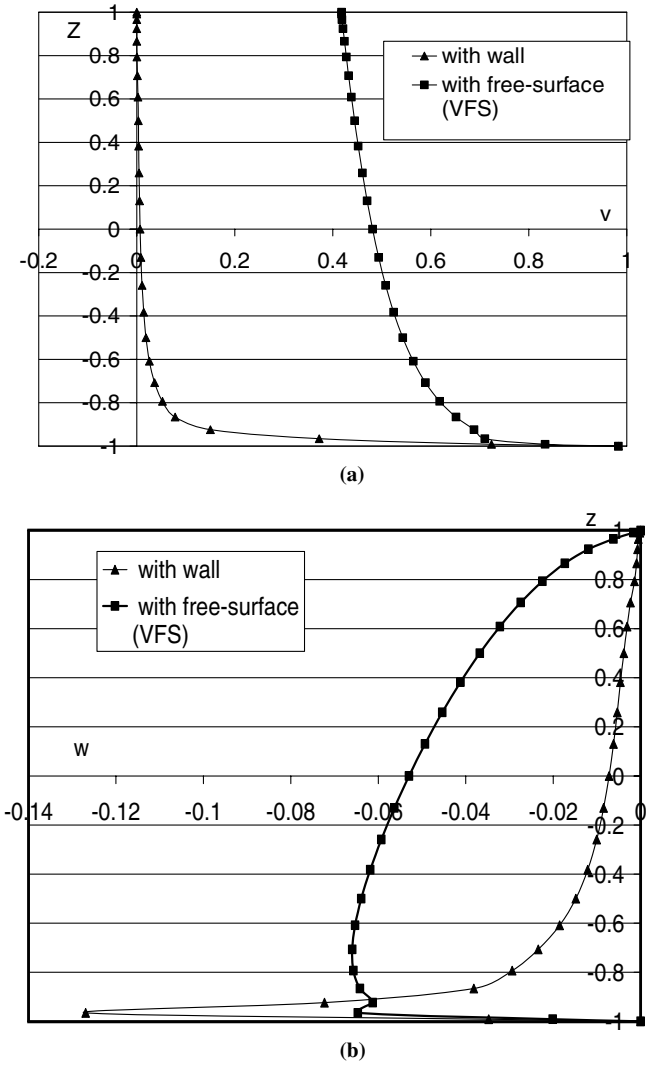

Fig. 18. Axial profiles of the azimuthal v (a) and axial w (b) velocity components at $Re = 1500$ at $r = 0.49$ along the vertical wall or free-surface (VFS).

gradient usually observed along the cylinder axis which is now close to zero. Indeed, the pressure is now almost constant between the bottom and the top of the cavity (Fig. 4(a)) and the vertical velocity is continuously accelerated along the axis to the rotating disk (Fig. 4(b)) due to the Ekman pumping of the rotating disk. In tune with this observation, no vortex breakdown has been obtained along the cylinder axis over the large range of Reynolds numbers considered in this study [500, 6000]. Moreover, the flow remains steady to very high Reynolds number estimated here at $Re = 6000$ and keeps the same organization as the one presented at $Re = 1500$ in Fig. 3(b). That shows that the transition to unsteadiness is governed by vertical boundary layer instabilities, at least below the critical Reynolds number of the Ekman layer.These results show that both the vortex breakdown process and the transition to unsteadiness in the cylinder are mainly governed by the non-parallel vertical layer developing along the wall container.

8. Concluding remarks

This study is the first to provide fully non-linear three-dimensional computations in a stationary cylindrical container of large aspect ratio $\Gamma = 4$, with a free-surface and a bottom rotating disk. Until now, direct numerical simulation in this large aspect ratio configuration has been mainly restricted to two-dimensional regimes which is very limiting specifically in the study of unsteady regimes. Experimental studies including a free surface are scarce because replacing the rigid cover by a free-surface makes the flow very sensitive, particularly for cylinders of large aspect ratios ($\Gamma > 3$). Consequently, measurements and analyses of flows in unsteady regimes are difficult.

The use of a spectral method coupled with a very efficient direct solver of the Navier–Stokes equations ensures high-order accuracy of these solutions. Modelling the free-surface with a simple, flat slip surface is shown to be adequate for the aspect ratio and for the range of Reynolds numbers considered in our study just below the chaotic regime. Indeed, at higher Reynolds number ($Re \geqslant 3150$) strong vortices develop just below the free-surface (Fig. 14) and then finite Froude-number effects should influence the solution, in particular the action of gravity in the deformation of free-surface (typically in experiments $Fr \approx 0.01$).

Our results show that substantial changes in the vortex breakdown properties can result from changing the upstream condition. One of the major characteristic of this flow is that the removal of the stationary disk boundary layer allows the attachment of the recirculation bubble to the free-surface. By removing the cylindrical vortex core upstream of the breakdown, this phenomenon modifies the usual properties of the vortex breakdown supposed in classical breakdown theories. The two stagnation points along the axis evolve into one stagnation line on the free-surface. This stagnation line forms a regular circle in the steady regime which evolves into a more irregular form that rotates around the axis in the direction of the rotating disk at larger Reynolds numbers. The transition from a steady axisymmetric to a multi-frequency three-dimensional regime occurs over a narrow range of Reynolds numbers [2900, 3150] via successive Hopf bifurcations related to rotating waves. The existence of a free-surface promotes the onset of unsteadiness, and the difference in the critical Reynolds number with and without a free-surface was estimated to be about 15%. The first bifurcation ($k = 3$) is related to the wall-jet flow produced near the cylindrical wall as previously suggested by Blackburn (2002) in the rigid cover configuration. As in the case with a rigid cover, the precessing motion of the vortex breakdown is associated to a $k = 1$ mode of instability. The mechanisms related to the $k = 1$ and 2 mode exhibited in our results require further investigation involving theoretical analysis of velocity profiles stability along the axis. In swirling jets, Billant et al. (1998) observed instability modes with the same wavelengths, suggesting that their theoretical

results might be extended in the present case. These modes of instability might be related to the helical disturbances observed in the tail of the bubble by Billant et al. (1998) and which break the axisymmetry of the bubble. This issue is left for further investigation.

Finally, our results show that no vortex breakdown is obtained over a large range of Reynolds numbers [500, 6000] when the container wall is replaced by an artificial slip-surface. That shows in particular, that some alterations in the adverse pressure gradient modify the breakdown process. Moreover, our results show that the stability of this flow is controlled by the vertical boundary-layer instabilities and that, without this boundary layer the flow remains steady over a large range of Reynolds numbers.

Acknowledgements

The authors acknowledge the IDRIS/CNRS (Orsay) computing centre where the computations were performed on Nec SX5 supercomputer (programme 040242).

References

Benjamin, T.B., 1962. Theory of the vortex breakdown phenomenon. J. Fluid Mech. 14, 593.

Billant, P., Chomaz, J.M., Huerre, P., 1998. Experimental study of vortex breakdown in swirling jets. J. Fluid Mech. 376, 183–219.

Blackburn, H.M., 2002. Three-dimensional instability and state selection in an oscillatory axisymmetric swirling flow. Phys. Fluids 14 (11), 3983–3996.

Blackburn, H.M., Lopez, J.M., 2000. Symmetry breaking of the flow in a cylinder by a rotating end wall. Phys. Fluids 12, 2698–2701.

Brøns, M., Voigt, L.K., Sørensen, J.N., 2001. Topology of vortex breakdown bubbles in a cylinder with a rotating bottom and a free-surface. J. Fluid Mech. 428, 133–148.

Crawford, J.D., Gollub, J.P., Lane, D., 1993. Hidden symmetries of parametrically forced waves. Nonlinearity 6, 119.

Daube, O., 1991. Numerical simulation of axisymmetric vortex breakdown in a closed cylinder. Lecture in Appl. Math. 28, 131.

Escudier, M.P., 1984. Observations of the flow produced in a cylindrical container by a rotating end wall. Exp. Fluids, 179–186.

Escudier, M.P., 1988. Vortex breakdown: Observations and explanations. Prog. Aerospace Sci. 25, 189–229.

Faler, J.H., Leibovich, S., 1977. Disrupted states of vortex breakdown. Phys. Fluids 19, 1285–1300.

Gelfgat, A.Y., Bar-Yoseph, P.Z., Solan, A., 2001. Three-dimensional instability of axisymmetric flow in a rotating lid-cylinder enclosure. J. Fluid Mech. 438, 363–377.

Gresho, P., Sani, R.L., 1987. On pressure boundary conditions for the incompressible Navier–Stokes equations. Int. J. Numer. Meth. Fluids 7, 137.

Hirsa, A.H., Lopez, J.M., Miraghaie, R., 2002. Symmetry breaking to a rotating wave in a lid-driven cylinder with a free-surface: Experimental observation. Phys. Fluids 14 (6), 29–32.

Hourigan, K., Graham, L.J.W., Thompson, M.C., 1995. Spiral streaklines in pre-vortex breakdown regions of axisymmetric swirling flows. Phys. Fluids 7 (12), 3126–3128.

Krause, E., 1990. The Solution to the Problem of Vortex Breakdown. In: Morton, K. (Ed.), Twelfth International Conference on Numerical Methods in Fluid Dynamics, Lecture Notes in Physics. Springer-Verlag, pp. 35–50.

Leibovich, S., 1978. The structure of vortex breakdown. Ann. Rev. Fluid Mech. 10, 221–246.

Lopez, J.M., Marques, F., Hirsa, A.H., Miraghaie, R., 2004. Symmetry breaking in free-surface cylinder flows. J. Fluid Mech. 502, 99–126.

Lucca-Negreo, O., O'Doherty, T., 2001. Vortex breakdown: A review. Prog. Energy Comb. Sci 27, 431–481.

Marques, F., Lopez, J.M., 2001. Precessing vortex breakdown in an enclosed cylinder flow. Phys. Fluids 13, 1679–1682.

Mullin, T., Kobine, J.J., Tavener, S.J., Cliffe, K.A., 2000. On the creation of stagnation points near straight and sloped walls. Phys. Fluids 12 (2), 425–431.

Pereira, J.C.F., Sousa, J.M.M., 1999. Confined vortex breakdown generated by a rotating cone. J. Fluid Mech. 385, 287–323.

Peyret, R., 2002. Spectral methods for incompressible viscous flowAppl. Math. Sci., 148. Springer-Verlag, New-York.

Pulicani, J.P., Ouazzani, J., 1991. A Fourier–Chebyshev pseudospectral method for solving steady 3-D Navier–Stokes equations in cylindrical cavities. Comp. Fluids 20, 93–109.

Raspo, I., Hugues, S., Serre, E., Randriamampianina, A., Bontoux, P., 2002. A spectral projection method for the simulation of complex three-dimensional rotating flows. Comp. Fluids 3, 745–767.

Rogers, M.H., Lance, G.N., 1960. The rotationally symmetric flow of a viscous fluid in the presence of an infinite rotating disc. J. Fluid Mech. 7, 617–641.

Sarpkaya, T., 1995. Turbulent vortex breakdown. Phys. Fluids 7 (10), 2301–2304.

Serre, E., Bontoux, P., 2002. Vortex breakdown in a three-dimensional swirling flow. J. Fluid Mech. 459, 347–370.

Serre, E., Pulicani, J.P., 2001. A 3D pseudospectral method for convection in a rotating cylinder. Comp. Fluids (30 / 4), 491–519.

Serre, E., Crespo del Arco, E., Bontoux, P., 2001. Annular and spiral patters in flow between rotating and stationary disks. J. Fluid Mech 434, 65–100.

Sørensen, J.N., Christensen, E.A., 1995. Direct numerical simulation of rotating fluid flow in a closed cylinder. Phys. Fluids 7, 764–778.

Sotiropoulos, F., Ventikos, Y., 1998. Transition from bubble-type vortex breakdown to columnar vortex in a confined swirling flow. Int. J. Heat Fluid Flow 19, 446–458.

Sotiropoulos, F., Ventikos, Y., 2001. The three-dimensional structure of confined swirling flows with vortex breakdown. J. Fluid Mech. 426, 155–175.

Sotiropoulos, F., Ventikos, Y., Lackey, T.C., 2001. Chaotic advection in three-dimensional stationary vortex-breakdown bubbles: Sil'nikov's chaos and the devil's staircase. J. Fluid Mech. 444, 257–297.

Sotiropoulos, F., Webster, D.R., Lackey, T.C., 2002. Experiments on Lagrangian transport in steady vortex-breakdown bubbles in a confined swirling flow. J. Fluid Mech. 466, 215–248.

Spohn, A., Daube, O., 1991. Recirculating flows in a cylindrical tank. In: Fifth International Conference on Computational methods and experimental Measurements, Montreal. Computational Mechanics Publications, Southampton, Boston, pp. 155–166.

Spohn, A., Mory, M., Hopfinger, E.J., 1993. Observations of vortex breakdown in an open cylindrical container with a rotating bottom. Exp. Fluids 14, 70–77.

Spohn, A., Mory, M., Hopfinger, E.J., 1998. Experiments on vortex breakdown in a confined flow generated by a rotating disc. J. Fluid Mech. 370, 73–99.

Young, D.L., Sheen, H.J., Hwu, T.Y., 1995. Period doubling route to chaos for a swirling flow in an open cylindrical container with a rotating disk. Exp. Fluids 18, 389–392.